modelling

MDPI

Article

Modeling the Production of Nanoparticles via Detonation—Application to Alumina Production from ANFO Aluminized Emulsions

Pedro M. S. Santos [1], Belmiro P. M. Duarte [1,2,3,*,†], Nuno M. C. Oliveira [1], Ricardo A. L. Mendes [4], José L. S. A. Campos [4], João M. C. Silva [5,6]

[1] Research Center for Chemical Engineering and Renewable Resources for Sustainability, Universidade de Coimbra, Rua Sílvio Lima—Pólo II, 3030-790 Coimbra, Portugal; nuno@eq.uc.pt
[2] Instituto Politécnico de Coimbra, Instituto Superior de Engenharia de Coimbra, Rua Pedro Nunes, 3030-199 Coimbra, Portugal
[3] INESC Coimbra—Instituto de Engenharia de Sistemas e Computadores de Coimbra, Universidade de Coimbra, Rua Sílvio Lima—Pólo II, 3030-790 Coimbra, Portugal
[4] ADAI-LAETA, Universidade de Coimbra, Rua Luís Reis Santos, Pólo II, 3030-788 Coimbra, Portugal
[5] Innovnano, Parque Tecnológico de Coimbra, 3040-540 Coimbra, Portugal
[6] Lifthium Energy, Rua do Silval 37, 12° piso, 2780-373 Oeiras, Portugal
* Correspondence: bduarte@isec.pt
† Current address: Polytechnic Institute of Coimbra, ISEC, Rua Pedro Nunes, 3030-199 Coimbra, Portugal.

Abstract: This paper investigates the production of nanoparticles via detonation. To extract valuable knowledge regarding this route, a phenomenological model of the process is developed and simulated. This framework integrates the mathematical description of the detonation with a model representing the particulate phenomena. The detonation process is simulated using a combination of a thermochemical code to determine the Chapman–Jouguet (C-J) conditions, coupled with an approximate spatially homogeneous model that describes the radial expansion of the detonation matrix. The conditions at the C-J point serve as initial conditions for the detonation dynamic model. The Mie–Grüneisen Equation of State (EoS) is used, with the "cold curve" represented by the Jones–Wilkins–Lee Equation of State. The particulate phenomena, representing the formation of metallic oxide nanoparticles from liquid droplets, are described by a Population Balance Equation (PBE) that accounts for the coalescence and coagulation mechanisms. The variables associated with detonation dynamics interact with the kernels of both phenomena. The numerical approach employed to handle the PBE relies on spatial discretization based on a fixed-pivot scheme. The dynamic solution of the models representing both processes is evolved with time using a Differential-Algebraic Equation (DAE) implicit solver. The strategy is applied to simulate the production of alumina nanoparticles from Ammonium Nitrate Fuel Oil aluminized emulsions. The results show good agreement with the literature and experience-based knowledge, demonstrating the tool's potential in advancing understanding of the detonation route.

Keywords: nanoparticle production; detonation modeling; Chapman–Jouguet conditions; Mie–Grüneisen equation of state; population balance equation; alumina nanoparticles

Citation: Santos, P.M.S.; Duarte, B.P.M.; Oliveira, N.M.C.; Mendes, R.A.L.; Campos, J.L.S.A.; Silva, J.M. C. Modeling the Production of Nanoparticles via Detonation—Application to Alumina Production from ANFO Aluminized Emulsions. *Modelling* **2024**, *5*, 1642–1673. https://doi.org/10.3390/modelling5040086

Academic Editor: Antonio Brasiello

Received: 11 October 2024
Revised: 31 October 2024
Accepted: 4 November 2024
Published: 7 November 2024

1. Introduction

The definition of the nanometric scale remains a topic of debate within the field of nanotechnology. Nonetheless, it is generally accepted that the nanometric scale ranges from 1 nm to 100 nm [1]. Within this range, it has been shown that material properties are influenced not only by their chemical composition but also by their size and shape. Over recent decades, it has been observed that properties such as optical, electrical, magnetic, hardness, toughness, and melting point of nanomaterials differ significantly from those of macroscopic solids [2].

In recent years, the use of nanoparticle-based materials has gained traction across various fields, including medicine [3,4], energy [5,6], military applications [7], and electronics [8], among others. Notably, there has been increased interest in the synthesis of nanoparticles and the development of control strategies to enhance quality and reproducibility. Despite progress, gaps in knowledge regarding the characterization and production of nanometric materials still exist. However, significant efforts in this area have largely met the goals for technological advancement and optimization, resulting in the market availability of materials that meet high expectations. Advances in processing methods and characterization techniques have enabled the controlled production of nanoparticles with diameters ranging from 1 nm to 10 nm, exhibiting consistent crystal structures and high levels of monodispersity [9].

Currently, research on nanoparticle synthesis processes is primarily focused on two broad areas: (i) gas-phase synthesis and (ii) sol-gel processing. Each of these areas encompasses several process routes that differ in terms of the technological devices required, degree of control achieved, and overall efficiency.

Sol-gel processing methods are based on wet chemical synthesis and include production strategies such as gelation, precipitation, and hydrothermal treatment [10]. These methods start with a chemical solution (sol phase), which acts as a precursor and transitions into a network (gel phase) of either discrete particles or polymeric entities [11]. Commonly used precursors include metal alkoxides and metal chlorides. The sol-gel approach offers several advantages, including economic benefits and the ability to fine-tune the chemical composition of the products due to its low-temperature requirements. This method is widely employed in ceramics processing and manufacturing, particularly for producing very thin films of metal oxides. The materials obtained through sol-gel processing find applications in various fields, including optics, electronics, energy systems, (bio)sensors, medicine, and separation technology [12,13].

Numerous sol-gel methods are well-documented in the literature, including sonochemical processing, cavitation processing, microemulsion processing, and high-energy ball milling. Sonochemical processing involves the production of nanoparticles through rapid changes in temperature and pressure within a closed chamber, triggered by sonochemical reactions. These sudden fluctuations arise from acoustic cavitation, which creates transient localized hot zones [14]. Cavitation processing, on the other hand, consists of a two-step procedure. First, gas bubbles are created and released within the sol-gel solution. The second step involves rapidly pressurizing the mixture in a supercritical drying chamber, where cavitation disturbances and temperature ramps are applied [15]. The bubbles act as nucleation sites and influence the physical mechanisms involved. Both the pressure and retention time in the cavitation chamber are adjustable parameters that control the particle size distribution (PSD). Microemulsion-based methods have been employed for synthesizing a variety of nanoparticles, including metallic [16], semiconductor [17,18], superconductor [19], silica [20], barium sulfate [21], and magnetic nanoparticles. The use of cosurfactants in these processes reduces the interfacial tension, allowing microemulsions to form spontaneously without significant mechanical agitation. This technique is advantageous for large-scale production due to lower hardware costs [22]. Finally, high-energy ball milling is utilized for producing magnetic [23], catalytic [24], and structural [25] nanoparticles. Although it is a widely available commercial technology, it is considered less desirable due to contamination issues and its high energy consumption. Additionally, it is a top-down processing route with drawbacks such as low surface area, highly polydisperse size distributions, and partially amorphous powders [26].

Despite the significance of sol-gel methods, many advancements in crystalline materials development rely on nanoparticles produced through evaporation and condensation processes, which involve successive nucleation and growth phenomena in a subatmospheric inert-gas environment [27–29]. At the industrial scale, micro- and nanoparticle synthesis is predominantly carried out using various methods [30], with gas-phase synthesis being particularly prevalent for producing metallic and alloy nanopowders [31]. According to

Rosner [32], gas-phase synthesis—utilizing gaseous, liquid, or even solid fuels—can offer significant economic advantages over sol-gel methods and other techniques (see also Zhao et al. [33]).

Recent developments have demonstrated that aerosol processing techniques are increasingly effective for improving nanoparticle production yields [34,35]. These techniques enhance the quality and cleanliness of the resulting powders through atomization, achieving higher conversion yields and particle size distributions within the nanometric range. Established synthesis techniques in the literature include the following: (i) combustion flame [36–38], (ii) plasma [39–42], (iii) laser ablation [43–46], (iv) chemical vapor deposition [47–49], (v) spray pyrolysis [50–53], (vi) electrospray [54–56], (vii) plasma spray [57–59], and (viii) detonation [60–63]. Comprehensive, up-to-date reviews on methods for synthesizing nanoparticles are available in Jamkhande et al. [64], Ndolomingo et al. [65], Pareek et al. [66].

In spite of the existence of several approaches for gas-phase synthesis-based routes, they all share the fundamental aspects of particle formation mechanisms:

1. Atomization of metallic species;
2. Oxidation of atomic entities in the gaseous phase;
3. Condensation of molecular critical aggregates;
4. Growth of the early formed aggregates.

The quality and application characteristics of nano-sized particles are strongly influenced by their size distribution and morphology [67,68]. In gas-phase reactors, the final characteristics of the particles are primarily determined by fluid mechanics and particulate dynamics within the initial milliseconds of the synthesis process. During this brief period, three dominant sequential mechanisms occur. First, the chemical reaction of precursors generates product monomers (clusters) by either nucleation or direct inception. These newly formed nuclei then grow as precursor molecules react on their surface [69,70]. Dispersed in a fluid phase, these entities move randomly due to Brownian motion, colliding and growing through coagulation driven by adhesive forces or chemical bonds characteristic of small particles [71,72].

In "hot-spot" zones of the reactors, the characteristic time of the coalescence mechanism is sufficiently short to reduce particle aggregation and promote the formation of spherical particles through sintering processes [73,74]. Each of these mechanisms significantly influences particle formation, growth, and final morphology, allowing for control of product quality through the careful selection of process set-points. However, due to the complex sequence of steps involved, which are challenging to describe mathematically, and the difficulty in monitoring process dynamics in these environments, establishing a direct relationship between process set-points (e.g., temperature, pressure, reactant state, and reactor geometry) and product characteristics is often problematic [2,75]. Moreover, gas-to-particle production routes can lead to challenges in preparing high-quality bulk materials when hard agglomerates form. The synthesis of multicomponent materials, such as phosphors and superconductors, is particularly difficult due to variations in chemical reaction rates, vapor pressures, nucleation, and growth rates during particle formation, commonly resulting in non-uniform compositions [76].

The detonation synthesis route, commonly used for producing nanodiamonds [77–79] and nanopowders [80–82], has recently been recognized as a promising approach for nanoparticle production [83]. This method involves placing an explosive matrix in a hermetically sealed chamber filled with oxygen-containing gases. The detonation reaction is initiated by a mechanical shock, which induces a sudden pressure increase that travels through the explosive matrix. Metallic components, used as precursors, are supplied in the form of an emulsion with the detonant matrix, whose primary role is to provide the energy needed for metal vaporization [84].

Nanoparticle generation using this technique follows a sequence of stages similar to those identified in general gas-to-particle routes. First, the detonation of the explosive matrix releases a large amount of energy, vaporizing both reaction products and inert materials, either partially or completely. At this stage, the vaporized metal undergoes

oxidation reactions, producing corresponding metal-oxide molecules. As aggregation and condensation of these metastable aggregates occur, the first stable liquid entities form and collide, driven by gas expansion and Brownian motion. Finally, in the last stage of the process, the nuclei grow mainly due to the coalescence of colliding particles until they solidify as the system temperature declines.

Despite the apparent simplicity of this process, as seen in systems such as the production of alumina nanoparticles (using metallic aluminum emulsified in detonation matrices), knowledge gaps regarding the mechanisms and phenomena involved are commonly reported in the literature. These gaps can affect the ability to control the final product quality [60].

The detonation route offers significant advantages over other gas-to-particle approaches. The substantial energy released during detonation, combined with the exceptionally fast reaction kinetics, results in steep increases in pressure and temperature. This maximizes the efficiency of species atomization. Consequently, the detonation route provides higher vaporization rates and higher saturation ratios of atomic species compared to other methods. This can be understood through the Kelvin–Gibbs relation [85]:

$$d_c = \frac{4\sigma V_m}{k_B T \ln(S)} \quad (1)$$

where d_c is the critical diameter of stable entities, $V_m = \frac{M}{N_A}$ is the molecular volume, $S = \frac{P^*}{P_s}$ is the saturation ratio, P^* is the vapor pressure at temperature T, P_s is the saturation pressure at the same temperature, σ is the surface tension, k_B is the Boltzmann constant, M is the molecular weight, and N_A is the Avogadro number. Given that the pressure and temperature points reached via detonation are higher than those in other gas-to-particle routes, the saturation ratio is also maximized. Consequently, the diameter of stable nuclei is smaller than that produced by any other technique.

However, this conclusion is theoretical. Despite numerous references using the Kelvin–Gibbs relation for prediction purposes (e.g., Friedlander [85], Sindhu et al. [86]), its application in real systems requires caution due to the scales and environmental conditions involved. It is commonly reported in the literature that this relation, based on thermodynamic principles, may fail for systems where particles form from very few molecules with non-rigid state transitions [85,87].

The higher saturation ratio achieved, combined with the short duration of the solidification time window, results in small, monodisperse particles, which can fall below the nanometric range [88]. This process also offers high production efficiency. Furthermore, the quasi-homogeneity of thermodynamic conditions in the detonation chamber during both the reaction and formation phases leads to low variability and a monodisperse PSD. Additionally, the rate of temperature decrease can potentially be controlled to influence particle growth [89]. Compared with other synthesis methods, detonation is a relatively ideal energy source because it can not only pulverize the powders effectively but also control granule growth within the limited time interval of the detonation reaction zone [90].

Despite the theoretical suitability of the detonation route for industrial nanoparticle production, its application has not been entirely successful due to issues with process reliability, reproducibility, and control over the final product characteristics, especially when using heterogeneous solid emulsions. Several authors attribute these drawbacks to the heterogeneity of the explosive matrix, which leads to the formation of local "hot-spots" where energy release preferentially occurs, resulting in unequal rates of atomization and local temperature gradients [91]. Additionally, the wide range of operating conditions, a major advantage of the detonation route over other gas-to-particle approaches, has not been fully exploited, limiting precise control over the process. The complexity of the reaction network leading to metallic oxides behind the shock front is not fully understood, and the mechanisms that achieve the desired product properties may be disrupted [92].

This knowledge gap between theory and industrial application hinders the reproducibility and control required for the detonation-based route to become a dominant industrial approach. Extracting knowledge from laboratory experiments is economically demanding and requires advanced technology and safety measures. Therefore, using phenomenological models combined with numerical algorithms, commonly employed by the Process Systems Engineering (PSE) community, can provide valuable insights.

This paper focuses on using first-principles-based models to describe the detonation process combined with Population Balance Equations to represent particulate phenomena. This approach aims to improve the understanding of the most relevant system variables, their influence on particle growth, and the ability to optimize both product and process. The literature on using PSE concepts to address nanoparticle generation and growth via detonation is scarce. To our knowledge, this is the first paper explicitly considering the influence of detonation features on particle size distribution (PSD).

While the conceptual basis developed here is intended to be applicable to any detonation system and precursor material, special attention is given to the formation of alumina nanoparticles from aluminum, with the detonant matrix being an Ammonium Nitrate Fuel Oil (ANFO) mixture composed of 59.41 % NH_4NO_3, 30.10 % Al, 6.97 % H_2O, 3.5 % Fuel, and 0.02 % Air (mol/mol fraction).

The paper includes five additional sections. Section 2 focuses on the theoretical basis and conceptualization of the detonation process, which is subsequently used to structure the model representing the behavior of intensive properties. Section 3 presents the mathematical model used to describe the phenomena affecting particle generation and growth, along with the numerical algorithms employed to handle the resulting Population Balance Equations (PBEs). Section 4 analyzes the simulation results obtained for the production of alumina nanoparticles. Finally, Section 5 summarizes the relevant conclusions regarding the use of the detonation-based route for producing metallic oxide nanoparticles.

2. Detonation Model

This section addresses the modeling of the detonation phenomenon used to transition metallic particles emulsified in an explosive matrix to the gas phase. A simplified conceptualization is proposed, and a dynamic model is derived to simulate the behavior of extensive properties interacting with particulate phenomena. The conceptual framework relies on axial homogeneity assumptions, coupled with radial homogeneity for all variables except radial expansion velocity, which is treated using a volume averaging method.

2.1. Process Conceptualization

This subsection presents the basic features related to the conceptualization of the detonation of an emulsion matrix comprising a detonator material and metallic particles in a sealed chamber, along with the assumptions used in model development. As mentioned in Section 1, the main goal is to enhance understanding of the key phenomena involved in nanoparticle production via detonation and to extract trends regarding process suitability that can be extrapolated to gas-to-phase routes. Since particulate process dynamics are crucial to achieving this goal and are directly influenced by the properties of the media, particularly the dependence of particle phenomena on the temperature and pressure of the explosive matrix—an accurate representation of the dominant features of the detonation is required.

The literature indicates that detonation process modeling can be approached with varying levels of detail [93,94], depending on the spatial and temporal scales used for phenomena representation and the phenomena included. More detailed models provide enhanced descriptions of dynamic features and better integrate different scales of phenomena but often result in significant numerical challenges. In this study, a simplified model is employed to capture the prevailing dynamics of detonation, with particular emphasis on understanding how extensive properties influence particulate phenomena. Given the current limited understanding of the interaction between the detonation process

and particulate phenomena, a basic representation of detonation is used to identify the most significant factors in nanoparticle formation and growth. In future work, if increased complexity is needed to enhance the predictive capability of the model for PSD of the final product, the model will be refined accordingly.

Moreover, the decision to use a simplified model for the detonation process also stemmed from the need to ensure numerical tractability. More advanced models, such as two-dimensional models accounting for time and axial dimension heterogeneity [95] and three-dimensional models [93], although offering greater predictive accuracy, would significantly increase both the complexity of the model and the computational resources required. This is particularly true when integrating with particulate-based phenomena descriptions.

The model developed for representing detonation phenomena is based on phenomenological conservation laws for mass, energy, and momentum. However, before delving into the specifics of the model, it is essential to clarify some fundamental concepts related to detonation theory. One of the foundational mathematical descriptions of detonation is the classic Chapman–Jouguet theory. For a comprehensive analysis of the C-J theory and its mathematical and physical aspects, readers are referred to Fickett and William [96] and Davidson [97]. The C-J theory describes detonation as an instantaneous transition of the particles in the detonation matrix from their initial state to the product state as a mechanically induced wave propagates through the material. The Equation of State for the products differs from that of the reactants, and the internal energy of the products includes the heat released during the reaction. The detonation reactions, characterized by rapid combustion transformations, are exothermic and release a substantial amount of energy. The shock wave at the reaction front adheres to "jump conditions" similar to those used to describe other non-reactive shocks. The core assumption of the C-J theory is that the reaction occurs so rapidly that it can be considered instantaneous.

From a steady-state perspective, the behavior of detonation products is represented by a curve connecting thermodynamic equilibrium points, depicting the sequence of states reachable from the shock transition departing from the reactants' state. These curves, which model the equilibrium loci of the products, are commonly referred to as Hugoniot curves. Relationships among Hugoniot curves, isotherms, and isentropes can be established. Depending on the monitored variables, Hugoniot curves exhibit different characteristics. Each material is defined by a family of Hugoniot curves, which can be obtained through laboratory tests. By combining Hugoniot curves with thermodynamic data, one can characterize the entropy and temperature changes occurring at the shock. The same considerations apply to isotherms and isentropes. In the detonation literature, straight lines connecting two states on a Hugoniot curve (or isotherm or isentrope) are known as Rayleigh lines.

In analyzing the detonation of a generic solid matrix using the $(p, \bar{v})$ plane, one can observe that the process begins with a sudden shock that initiates the reaction, transforming the reactants from an initial state $(p_0, \bar{v}_0)$ into gaseous reaction products in equilibrium at $(p_1, \bar{v}_1)$. Here, p_i denotes the system's pressure in state i, and $\bar{v}_i$ represents the corresponding molar volume.

In detonation systems, despite the sequential solid–liquid–gas transformations, significant pressure increases from state 0 to state 1 are observed, with pressure values on the order of a few GPa reported in the literature, coupled with reductions in molar volume. Subsequently, the gas products expand along a Hugoniot curve. The state immediately behind the detonation shock lies at the tangency of the Hugoniot curve with the Rayleigh line, defined by $(p_1, \bar{v}_1)$. When the Hugoniot and Rayleigh curves meet tangentially at a single point, this point is called the Chapman–Jouguet (C-J) point, denoted as $(p_{CJ}, \bar{v}_{CJ})$. Figure 1 illustrates this sequence of state transitions.

In this work, we address the dynamics of the gaseous matrix expansion starting from the Chapman–Jouguet (C-J) point. This assumption implies that the C-J point serves as the initial time for the dynamic simulation. Consequently, it is assumed that the entire explosive matrix has already reacted, with the detonation wave having reached the end

of the solid matrix, and the products are in the gaseous phase. The transition from the initial state of reactants to the C-J point is mathematically resolved using the steady-state "jump conditions" of the Chapman–Jouguet theory, combined with a thermochemical code to estimate the reaction heat. For this purpose, the THOR platform, a thermochemical code for predicting detonation product properties, is employed [98]. Therefore, the dynamic model presented in the following section describes the evolution of system properties after complete detonation of the explosive matrix, based on conservation laws. This assumption also eliminates the need for an Equation of State (EoS) for the explosive material in its solid state.

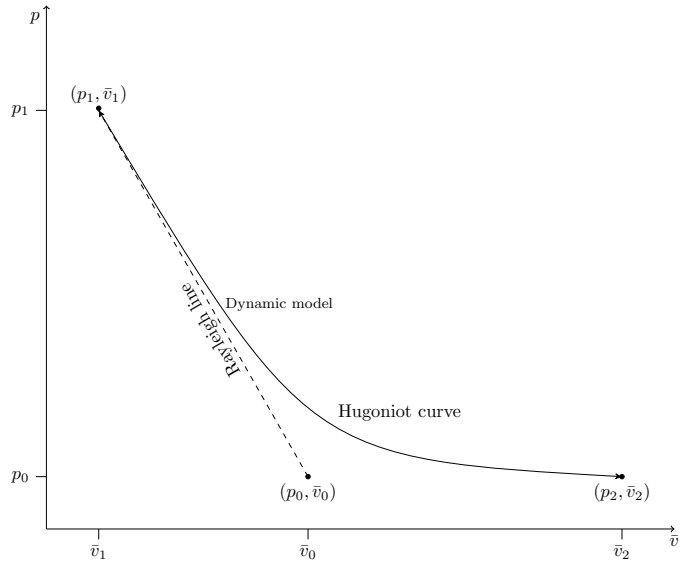

Figure 1. Schematic representation of transformations in the $p - \bar{v}$ plane.

The Chapman–Jouguet theory treats the C-J point as the singular point where thermodynamic equilibrium is achieved behind the reaction front, despite the detonation front being modeled as a mathematical/physical discontinuity. Another assumption arising from the C-J theory is that the detonation front moves across the solid matrix with nearly flat spatial geometry. Behind the rarefaction wave following the detonation front, the gaseous products expand isentropically, driven by the pressure gradient between the system and its surroundings (air at atmospheric pressure). In our model, the detonation matrix is cylindrical, and expansion is considered to occur only in the radial direction, with changes in the x-dimension being neglected. Thus, the expansion system is modeled as a front with radial displacement, where the pressure in the chamber drives the radial expansion velocity. This front is associated with large pressure gradients, as the pressure inside the expanding cylinder reaches very high values while the surrounding medium remains at atmospheric pressure. The physical description of this gas expansion process results in a moving boundary problem, which is numerically challenging [99,100]. In this study, the dynamics of the moving front and continuity conditions are not explicitly addressed. Instead, the radial position of the boundary, denoted as the outer layer, is determined based on the radial velocity, and pressure dynamics are described using the momentum conservation law combined with the EoS.

Another crucial aspect of the dynamic model is the characterization of the expansion velocity. The system is conceptually represented as a series of cylinders with infinitesimal thickness, each considered independent of the others (see Figure 2). For a given cylinder, its properties and their variations over time do not affect adjacent cylinders. Therefore, pressure dynamics in one cylinder do not influence neighboring cylinders, an assumption that results from neglecting axial expansion. All cylindrical elements are assumed to exhibit similar behavior, transitioning through the same thermodynamic states as the detonation front progresses axially along the explosive but with a time lag proportional

to the detonation velocity. Since the cylinders are characterized by similar dynamics, the properties within the detonation matrix are well represented by the dynamics of a generic infinitesimal thickness cylinder, which is considered the basic volumetric entity for modeling. Moreover, successive thermodynamic equilibriums are assumed to be achieved instantaneously using an EoS to model the system's thermodynamic variables.

Additionally, the dynamics of properties within each infinitesimal cylinder, except for radial velocity, are considered independent of the radial position. Thus, variables representing the dynamics in each cylinder (pressure, density, and specific internal energy) are global. To prevent inner layers from surpassing outer layers due to higher radial velocities, the cylinder is conceptualized as a series of concentric rings, each expanding at a velocity proportional to the outermost ring. This approach prevents particles in inner concentric rings from overtaking those in outer rings with higher radial velocities (see Figure 2). The model describes the radial velocity expansion of the outer ring, which is then used to compute a volumetric-weighted velocity for the entire cylinder. This consideration is particularly important for calculating the kinetic energy term.

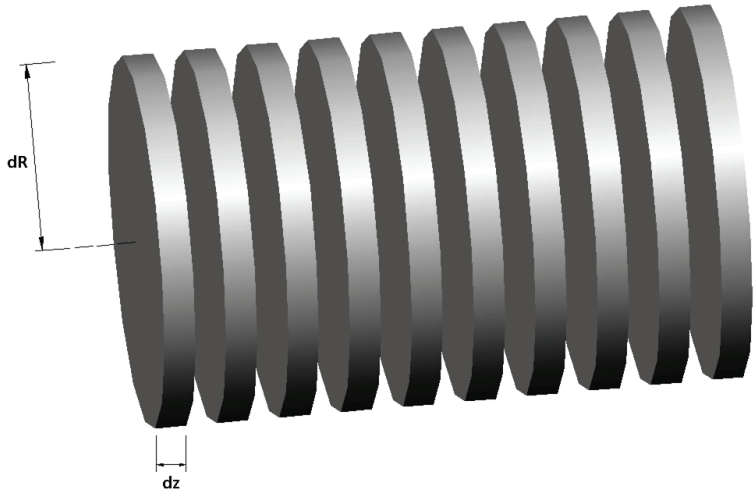

Figure 2. Conceptual model of the system, consisting of a set of infinitely thin, mutually independent cylinders.

In summary, the dynamic model assumes both axial and radial homogeneity for extensive properties, with the exception of the radial velocity of expansion. The system is conceptualized as a series of infinitesimally thin cylinders, each with uniform extensive properties. These cylinders are composed of infinite concentric rings that expand in a coordinated manner, maintaining consistent relative radial positions throughout the expansion.

2.2. Phenomenological Model

Most studies in the literature that develop phenomenological models for simulating detonation dynamics tend to overlook the radial expansion velocity of the products after reaching the C-J point [101]. However, for the goals of this work, accurately characterizing the expansion velocity is crucial, as it influences the dynamic evolution of system properties and the period of particle coalescence. Intuitively, the dynamic model for the radial expansion velocity depends on the differences between conditions inside the cylinder defined by the outer ring and the surrounding medium. To our knowledge, there are two main methodologies for determining this radial expansion velocity:

- Simulation of the detonation phenomenon post-C-J point using heterogeneous three-dimensional models (accounting for time, axial, and radial dimensions), which solve momentum balances in both the axial and radial directions. This approach assumes irrotational movement to determine the radial expansion velocity [102].

- Application of semi-empirical relations based on the foundational work of Wood and Kirkwood [103], specifically adapted to central flow lines [104].

Due to the one-dimensional nature of our model, we use the latter approach. Despite the empirical nature of these relations, they include a term theoretically supported by a force balance applied to the boundary layer of the expanding cylinder [105–107].

According to the system conceptualization introduced in Section 2.1, the radial expansion velocity of each ring is given by

$$u_r = \frac{r}{R} u_R, \quad 0 \leq r \leq R \tag{2}$$

where r is the radius of the ring expanding with velocity u_r and R is the radius of the cylinder's boundary layer expanding with velocity u_R.

A momentum balance at the boundary layer yields the following equation for the radial expansion velocity of the outer ring, whose radius is $R(t)$:

$$\frac{\mathrm{d}u_R}{\mathrm{d}t} = \frac{2(p - p_0)}{\rho R} \tag{3}$$

where p denotes the pressure of the expanding medium, p_0 is the pressure of the surrounding medium (typically gaseous), and ρ represents the density of the expanding medium. This equation, initially used by Lu et al. [104], aligns with the theoretical framework proposed by Wood and Kirkwood [103]. Their work provides a theoretical basis for the detonation phenomenon, incorporating both radial and axial components of the products' velocity. They demonstrate that a two-dimensional representation of the velocity is valid for the central flow line.

Although we assume negligible axial expansion, we use a similar paradigm to model the boundary velocity at time $t = 0$ (C-J point) with

$$u_R(t = 0) = \frac{D_{CJ} - u_{CJ}}{R_c} R_{CJ}. \tag{4}$$

Here, D_{CJ} is the detonation wave velocity along the axial direction of the explosive matrix, u_{CJ} is the sonic velocity of the detonation wave, and R_{CJ} is the explosive radius at the C-J point. R_c represents the curvature radius of the detonation front, given by

$$R_c = \frac{R_0}{\tan(\theta)} \tag{5}$$

where R_0 is the explosive radius at point 0 and θ is the angle between the explosive axis and the normal to the shock front. The value of θ is characteristic of the explosive configuration and is listed for common matrices [108].

Assuming the expanding system is isolated with no mass losses, the dynamics of the fundamental volumetric entity can be described by a mass conservation equation. Taking the C-J point as the reference, the mass balance equation is

$$\rho_{CJ} V_{CJ} = \rho(t) V(t) \tag{6}$$

where ρ_{CJ} and V_{CJ} are the density and volume of the system at the C-J point, respectively, and $\rho(t)$ and $V(t)$ represent the density and volume at a generic time t. The evolution of the system's volume can be traced using the relation

$$\mathrm{d}V(t) = \pi \cdot R^2(t) \cdot \mathrm{d}z \tag{7}$$

where $\mathrm{d}z$ denotes the infinitesimal thickness of the cylindrical elements. Given the conceptual assumptions about the coordinated movement of the concentric rings comprising each

cylindrical element, the system's volume is determined by the radial expansion velocity of the outer layer. This is described by

$$\frac{\mathrm{d}R(t)}{\mathrm{d}t} = u_R(t) \tag{8}$$

with the initial condition $R(0) = R_{CJ}$. From this point onwards, the notation "(0)" refers to the initial state, corresponding to $t = 0$.

To characterize the energy dynamics of the expanding system, we use the enthalpy conservation law, considering kinetic, mechanical, and internal energy terms. It is assumed that the enthalpy of the system remains constant relative to the reference C-J point.

Over time, transformations occur, converting mechanical and internal energy into kinetic energy. Consequently, the energy balance in terms of mechanical energy can be expressed as

$$e_{CJ} + \frac{p_{CJ}}{\rho_{CJ}} + K_{CJ} = e(t) + \frac{p(t)}{\rho(t)} + K(t) \tag{9}$$

where K_{CJ} and $K(t)$ represent the kinetic energy, e_{CJ} and $e(t)$ denote the specific internal energy, and the ratios $\frac{p_{CJ}}{\rho_{CJ}}$ and $\frac{p(t)}{\rho(t)}$ correspond to the shaft work at the C-J point and at a given time t, respectively.

Considering the earlier assumptions regarding system expansion, the overall kinetic energy is the sum of the contributions from all concentric rings. Thus, the kinetic energy at time t is given by

$$K(t) = \frac{1}{\pi\, \rho(t)\, R(t)^2\, \mathrm{dz}} \int_0^{R(t)} 2\pi\, \rho(t)\, r\, u_r^2(t)\, \mathrm{dz}\, \mathrm{d}r = \frac{1}{4} u_R^2(t). \tag{10}$$

The values of the variables at the C-J point used in Equations (4)–(9)—namely, ρ_{CJ}, p_{CJ}, and e_{CJ}—are obtained from a thermochemical prediction platform. Similarly, the values of V_{CJ} and R_{CJ} are determined based on the mass of the detonation matrix and $\bar{v}_{CJ} = \frac{1}{\rho_{CJ}}$. To close the system of Differential-Algebraic Equations (DAEs), two additional equations are required. These equations arise from a $p - \bar{v} - e$ EoS describing the thermodynamic equilibrium loci. We use the Mie–Grüneisen $p - \bar{v} - e$ EoS, commonly employed for systems involving condensed matter or solids [109]. This EoS is given by

$$p(V, e) - p_k(v_s) = \frac{\omega}{V}[e - e_k(v_s)] \tag{11}$$

where $p(V, e)$ is the pressure in equilibrium with the volume V and specific internal energy e, p_k is the reference pressure, e_k is the reference specific internal energy, and e is the specific internal energy corresponding to $p(V, e)$. The scaled specific volume v_s is defined as $v_s = \frac{\bar{v}}{\bar{v}_0} = \frac{\rho_0}{\rho}$, where $\bar{v}_0$ is the reference specific volume. The parameter ω is the Grüneisen coefficient, with $\omega = \gamma + 1 = \frac{C_p}{C_v} + 1$ for ideal systems.

In detonation systems involving condensed matter, such as the one under consideration, the 0 K isotherm, often referred to as the cold compression curve, is commonly used as a reference curve. The specific internal energy is derived by adding a thermal energy term to the elastic energy represented by the cold isotherm at 0 K.

This paper employs two different Equations of State (EoSs) to describe the cold isotherm. The first is the Jones–Wilkins–Lee (JWL) EoS, which combines two Murnaghan EoSs and one Taft EoS, involving a total of six parameters [110]. The JWL EoS is known for its strong predictive capability across a wide range of conditions typical in detonation processes [111]. Specifically, one Murnaghan EoS provides an accurate fit for high-pressure conditions, the other is suited for intermediate pressures, and the Taft EoS offers a reliable prediction for low pressures.

In this work, a simplistic polytropic Equation of State is also employed to analyze the influence of the Jones–Wilkins–Lee (JWL) EoS on detonation dynamics. Both EoSs consid-

ered are commonly referred to as γ-variable EoSs. For gaseous systems, this assumption enhances the quality of simulation results, and theoretical equations for computing γ and updating its value over time are available in the literature [112]. However, in simulations involving solid matrices, particularly when gaseous mixtures with condensed matter are present, several authors use constant γ values [113]. This assumption is also adopted in this paper.

Here, the JWL EoS is represented as follows (see Massoni et al. [114]):

$$p_k(v_s) = p_{k1}(v_s) + p_{k2}(v_s) \tag{12a}$$

$$p_{k1}(v_s) = A\exp(-C_1 v_s) + B\exp(-C_2 v_s) \tag{12b}$$

$$p_{k2}(v_s) = k v_s^{-(\omega+1)} \tag{12c}$$

$$k = \left[p_{CJ} - p_{k1}(v_{CJ}) - \frac{\omega C_v T_{CJ}}{\bar{v}_{s,CJ}}\right] v_{s,CJ}^{\omega+1} \tag{12d}$$

$$e_k(v_s) = e_{k1}(v_s) + e_{k2}(v_s) \tag{12e}$$

$$e_{k1}(v_s) = \left[\frac{A\exp(-C_1 v_s)}{C_1} + \frac{B\exp(-C_2 v_s)}{C_2}\right]\bar{v}_0 + c_{ek} \tag{12f}$$

$$e_{k2}(v_s) = \frac{k\bar{v}_0}{\omega} v_s^{-\omega} \tag{12g}$$

$$c_{ek} = -\left[\frac{A\exp(-C_1 v_{s,CJ})}{C_1} + \frac{B\exp(-C_2 v_{s,CJ})}{C_2}\right]\bar{v}_0 - \left[\frac{p_{CJ} - p_{k1}(v_{s,CJ})}{\omega}\right]\bar{v}_{CJ} + e_{CJ} \tag{12h}$$

All variables retain the meanings introduced previously, with $v_{s,CJ}$ representing the scaled specific volume at the C-J point and C_v denoting the specific heat of the expansion matrix at constant volume. The constants A, B, C_1, C_2, and ω are specific to the detonation matrix and are typically determined through fitting data obtained from cylinder tests. For this study, values for these constants were sourced from the literature for ANFO [115]. The parameters k and c_{ek} are adjusted based on the values of the variables at the C-J point, as determined by the thermochemical code. The goal is to achieve an isentropic curve that intersects the C-J point. In this context, the constant k represents the mechanical energy expressed as pressure on the cold compression curve [116]. Similarly, c_{ek} accounts for the increase in mechanical energy at the C-J point due to the heat released from the reaction.

When using the polytropic EoS, the modifications involve setting $p_{k1}(v_s)$ and $e_{k1}(v_s)$ to zero. According to Fickett and Wood [117], temperature is not required or known for simulating detonation processes. However, in our case, temperature, along with pressure, significantly affects particulate phenomena, and thus its dynamics must be modeled, simulated, and integrated into the framework.

Temperature is crucial because the velocity of particle coalescence depends on it, and monitoring the temperature decrease is essential to determine when it falls below the solidification temperature of the material (alumina oxide, in this case), which halts growth. The specific internal energy, particularly when using a cold compression curve as a reference, helps quantify the thermal component and determine the corresponding temperature. Several relationships in the literature connect isentropes, isotherms, and Hugoniot curves [97]. These relationships enable the determination of temperature using a reference curve. In this study, we employ one such relationship, also used in works such as Menikoff [118]:

$$T(t) = \frac{e(t) - e_k(t)}{C_v} \tag{13}$$

Here, $T(t)$ is the temperature at time t, $e(t)$ is the specific internal energy at time t, $e_k(t)$ is the specific internal energy at the reference point, and C_v is the specific heat capacity at constant volume.

The empirical equation used to determine the vapor pressure of liquid-phase alumina is provided by [119]

$$P(T_{sol}) = 1.3176 \times 10^4 \left[\left(\frac{T_{sol}}{2200} \right)^{6.24} - 1 \right] \quad (14)$$

where P represents the system pressure (in bar) and T_{sol} is the solidification temperature (in K).

3. Particulate Dynamics

This section focuses on modeling the particulate phenomena involved in the formation and growth of metallic oxide droplets. After the detonation, the energy released from the reaction vaporizes the metallic components present in the matrix. The vaporized metallic species then react with oxygen (or other chemical species) to form metallic oxides, such as alumina in our case, which initially exist as individual molecules. At this stage, the gaseous phase is rich in metallic oxide vapor. As the pressure and temperature decrease, the vapor condenses to form nuclei of critical size. These nuclei eventually coalesce into liquid droplets when saturation conditions are met.

The transformations described occur instantaneously up to the C-J point. Beyond this point, the metallic droplets begin to collide with each other, leading to increased particle size due to coalescence and coagulation phenomena. Coalescence refers to the process where two spherical particles merge to form a larger spherical particle upon collision. The resulting particle has minimal surface energy, with its volume equal to the sum of the original particles' volumes [120]. Coagulation, on the other hand, involves the aggregation of droplets without amalgamation. Although coagulated droplets may not be spherical, their characteristic dimension is represented by the equivalent sphere.

Once the solidification temperature of the metallic oxide material is reached, the droplets transition to a solid state, and their characteristic dimension ceases to increase. Consequently, the simulation time domain covers the interval from the C-J point until the transition from liquid to solid for the metallic oxide droplets occurs. The rates of coagulation and coalescence depend on the system's temperature and pressure, which are influenced by the expansion of the detonation matrix as described in Section 2. These variables interact with the particulate phenomena [121]. However, we assume that the PSD does not affect the detonation dynamics.

3.1. Population Balance Equation Representation

The Particle Balance Equation (PBE) is characterized in the literature as a system of integro-partial differential equations [122]. These equations incorporate terms commonly used to describe various particulate phenomena. Spatial dependence arises from modeling the particle distribution as a spatial representation of the characteristic dimension, which describes the frequency of occurrence of particles (e.g., diameter, volume). Time dependence captures the accumulation of particles, particularly addressing growth and nucleation phenomena. Integral terms account for aggregation, coalescence, breakage, and coagulation processes.

The PBE models the probability density function (pdf), denoted as $F(x)$, representing the number of particles whose characteristic dimension lies within the infinitesimal interval $[x; x + \mathrm{d}x]$. In our system, the characteristic dimension is the particle size, which can be expressed in terms of diameter (assuming spherical particles), volume, surface area, or mass. For this case, these metrics are inherently correlated.

The theory and solution methods for general PBEs are detailed in several references, such as Hulburt and Katz [123], Randolph [124], Ramkrishna [125,126], Kumar and Ramkrishna [127,128]. The general form of the PBE for a given particle distribution $F(x)$ is expressed as

$$\frac{\partial F(x,t)}{\partial t} = \underbrace{\frac{\partial}{\partial x}\left(\frac{\mathrm{d}x}{\mathrm{d}t}\cdot F(x,t)\right)}_{\substack{\text{growth of}\\ \text{particles of size } x}} + \underbrace{\delta_d(x-x_N)\cdot R_N(t)}_{\substack{\text{nucleation of new}\\ \text{particles of size } x_N}} + \underbrace{\int_x^\infty k_b(u)\cdot g(u,x)\cdot F(u,t)\cdot \mathrm{d}u}_{\substack{\text{formation rate of particles of size } x\\ \text{due to the break of size } u>x}} +$$
$$+ \underbrace{\frac{1}{2}\int_0^x \beta(x-u,u)\cdot F(x-u,t)\cdot F(u,t)\cdot \mathrm{d}u}_{\substack{\text{formation rate of particles of size } x \text{ due to the}\\ \text{coalescence of particles of size } u \text{ and } x-u}} - \underbrace{F(x,t)\cdot k_b(x)}_{\substack{\text{consumption rate of particles}\\ \text{with size } x \text{ due to breakage}}} - \underbrace{F(x,t)\cdot\int_0^x \beta(x,u)\cdot F(u,t)\cdot \mathrm{d}u}_{\substack{\text{consumption rate of particles with size } x\\ \text{due to coalescence with particles with size } u}} \quad (15)$$

Here, $k_b(u)$ represents the number of particles produced from breaking particles of size u per time unit, $g(u,x)$ is the breakage kernel describing the probability of forming a particle of size x from breaking particles of size u per time unit, $\beta(x-u,u)$ is the coagulation/coalescence kernel representing the collision frequency between particles of sizes $x-u$ and u per time unit, $\delta_d(\bullet)$ is the Dirac delta function, $R_N(t)$ is the nucleation rate of new particles of critical size x_N, and $\frac{\mathrm{d}x}{\mathrm{d}t}$ is the growth rate of particles of size x.

The complexity of Equation (15), which involves specific initial distributions and kernel representations, often precludes obtaining an analytical solution. As a result, numerical methods are typically the only viable approach for simulating the dynamic behavior of the particle size distribution.

In our modeling of droplet PSD dynamics, the growth term is omitted because the rate of metallic layer deposition onto the nuclei is negligible compared to the rapid expansion of the system. Similarly, the nucleation term is excluded, as we assume that all droplet condensation occurs almost instantaneously. The partial pressure of metallic oxides in the vapor phase decreases sharply, reducing the likelihood of new nucleus formation during matrix expansion [89].

Additionally, the breakage terms are disregarded under the assumption that droplet collisions result in amalgamation or aggregation rather than fragmentation. We focus on two mechanisms that contribute to the increase in particle size: (i) coalescence and (ii) coagulation. Thus, the PSD dynamics are primarily governed by the coalescence and coagulation of liquid metal droplets, with coagulation specifically included to align with empirical data obtained from industrial laboratory tests.

To simplify the analysis of the Partial Balance Equation (PBE) and the presentation of the numerical strategy employed, a model focusing solely on coalescence is used, given that coalescence and coagulation are described by similar representations and kernels. Extending the treatment to include both coalescence and coagulation phenomena is straightforward. The general PBE describing the dynamics of metallic droplets until solidification, incorporating the aforementioned simplifications and assumptions, is given by

$$\frac{\partial F(x,t)}{\partial t} = \frac{1}{2}\int_0^x \beta^l(x-u,u)\cdot F(x-u,t)\cdot F(u,t)\cdot \mathrm{d}u - F(x,t)\cdot\int_0^\infty \beta^l(x,u)\cdot F(u,t)\cdot \mathrm{d}u, \quad (16a)$$
$$F(x,0) = F^0(x), \quad (16b)$$

where $\beta^l(x-u,u)$ is the coalescence kernel and $F^0(x)$ is the initial PSD. The kernel also depends on system properties like temperature and pressure, influencing the particle collision dynamics. The $\frac{1}{2}$ factor in the first term of Equation (16) avoids double counting the same pair of particles [85].

To account for simultaneous coalescence and coagulation, the PBE extends to

$$\frac{\partial F(x,t)}{\partial t} = \frac{1}{2}\int_0^x \beta^l(x-u,u)\cdot F(x-u,t)\cdot F(u,t)\cdot \mathrm{d}u - F(x,t)\int_0^\infty \beta^l(x,u)\cdot F(u,t)\cdot \mathrm{d}u +$$
$$+ \frac{1}{2}\int_0^x \beta^g(x-u,u)\cdot F(x-u,t)\cdot F(u,t)\cdot \mathrm{d}u - F(x,t)\cdot\int_0^\infty \beta^g(x,u)\cdot F(u,t)\cdot \mathrm{d}u, \quad (17a)$$
$$F(x,0) = F^0(x), \quad (17b)$$

where $\beta^g(x-u,u)$ represents the coagulation kernel.

Equations (16) and (17) conceptually describe particulate dynamics. For adaptation to our system, we define the characteristic dimension of droplets as their volume, denoted by v. The pdf of droplets of different volumes is represented by classes $N(v,t)$, which denotes the number of droplets with volumes in the range $[v, v+\mathrm{d}v]$ in the detonation volume at time t. Specifically, $N(v,t)$ is given by $V(t)\cdot n(v,t)$, where $V(t)$ is the volume of the detonation system at time t (see Equation (7)), and $n(v,t)$ is the concentration of particles within the infinitesimal volume interval $[v, v+\mathrm{d}v]$.

Partial Balance Equations are often formulated for systems where the reaction volume remains constant over time. However, in our case, the reaction volume continuously increases due to the expansion of the detonation matrix described in Section 2. This expansion leads to a rarefaction of colliding entities, thereby affecting the collision probability and consequently the dynamics of the PSD. Considering these factors, Equation (16) becomes

$$\frac{\partial n(v,t)}{\partial t} = \frac{1}{2}\int_0^v \beta^l(v-u,u)\cdot n(v-u,t)\cdot n(u,t)\cdot \mathrm{d}u - n(v,t)\cdot\int_0^\infty \beta^l(v,u)\cdot n(u,t)\cdot \mathrm{d}u - \frac{n(v,t)}{V(t)}\cdot\frac{\mathrm{d}V(t)}{\mathrm{d}t} \tag{18a}$$

$$n(v,0) = n^0(v), \tag{18b}$$

where $\frac{\mathrm{d}V(t)}{\mathrm{d}t} = 2\pi R(t) L \frac{\mathrm{d}R(t)}{\mathrm{d}t}$ is the rate of volumetric expansion and $\frac{\mathrm{d}R(t)}{\mathrm{d}t}$ is given by Equation (3). Similarly, Equation (17) extends to

$$\begin{aligned}\frac{\partial n(v,t)}{\partial t} = {} & \frac{1}{2}\int_0^v \beta^l(v-u,u)\cdot n(v-u,t)\cdot n(u,t)\cdot \mathrm{d}u - n(v,t)\cdot\int_0^\infty \beta^l(v,u)\cdot n(u,t)\cdot \mathrm{d}u + \\ & + \frac{1}{2}\int_0^v \beta^g(v-u,u)\cdot n(v-u,t)\cdot n(u,t)\cdot \mathrm{d}u - n(v,t)\cdot\int_0^\infty \beta^g(v,u)\cdot n(u,t)\cdot \mathrm{d}u - \frac{n(v,t)}{V(t)}\cdot\frac{\mathrm{d}V(t)}{\mathrm{d}t},\end{aligned} \tag{19a}$$

$$n(v,0) = n^0(v). \tag{19b}$$

Two aspects of PBEs (18) and (19) are further clarified in the next subsections. The first is the representation of the kernels for both phenomena, and the second is the initial PSD distribution, $n^0(v)$.

3.2. Coalescence/Coagulation Kernel

At first glance, the analysis of the coalescence phenomenon between metallic liquid droplets suggests that it would occur in a turbulent regime, driven by the violent detonation of the explosive charge. However, this assumption would contradict some of the considerations used earlier in modeling the expansion of detonation products. The effects of gas viscosity in a turbulent regime cannot be neglected, making it unreasonable to assume the absence of radial profiles of the intensive properties that characterize the system.

Considering the magnitude of the speed at which the particles move during the expansion process, if a balance between inertial and viscous forces is derived, the viscous term can be neglected. Physical reasoning leads us to consider that the coalescence phenomenon is dominated by the particles' Brownian motion. Therefore, the kernel employed must reflect the features of this regime. The literature on kernel representations for particulate processes dominated by coalescence in Brownian motion systems is extensive. The choice of the most appropriate function for a particular system depends on the ratio between the particle diameter, d_p, and the mean free path of the gas, ℓ [85], which is defined as the average distance traveled by a gas molecule between successive collisions [129]:

$$\ell(t) = \frac{V_m(t)}{\pi\, d_p^2\, N_A} \tag{20}$$

where all variables have their previously introduced meanings, and $V_m(t) = \frac{M_m}{\rho(t)}$, with M_m representing the mass of the detonation matrix. Determining the mean free path of the gas

in the vapor mixture requires the average molecular weight and gas particle diameter. The composition of the gaseous phase at the C-J point, determined by the thermochemical code, is used to calculate these properties.

The relationship between particle diameter and the mean free path determines whether the system falls into the continuous regime ($d_p \gg \ell$) or the free molecular regime ($d_p \ll \ell$) [85]. Another strategy to infer the dominant motion regime of the expanding droplets is to determine the Knudsen number, Kn, defined as the ratio of the mean free path of the gas to the characteristic size (here, the diameter of alumina droplets). The Knudsen number helps determine whether the fluid dynamics framework should be based on statistical mechanics ($Kn \geq 0.1$) or continuum mechanics ($Kn < 0.1$) [129].

To illustrate the calculation scheme, a detonation system based on an ANFO matrix with emulsified metallic aluminum is considered, with variable values at the C-J point and vapor composition obtained via the THOR platform. Table 1 presents the results for a matrix with an initial diameter of 5 cm and a length of 3 cm. The simulation assumes the chamber is initially at 25 °C and 1 atm. The results in Table 2 indicate that the system can be addressed using continuum mechanics.

Table 1. Data acquired from THOR simulation of the production of alumina nanoparticles via detonation of 1 kg of explosive matrix. The values presented are for the pre-detonation state, designated earlier by the underscript 0, and at the C-J point, denoted by the underscript C-J, respectively.

Initial Conditions					
$P_0 = 1.0$ kbar	$T_0 = 298$ K	$V_0 = 0.800\,\mathrm{cm^3/g}$	$\rho_0 = 1249.72\,\mathrm{kg/m^3}$		
Conditions at the C-J Point					
$P_{CJ} = 149.015$ kbar	$T_{CJ} = 4370.223$ K	$V_{CJ} = 0.603\,\mathrm{cm^3/g}$	$\rho_{CJ} = 1658.37\,\mathrm{kg/m^3}$	$Cv_{CJ} = 2502.393\,\mathrm{kJ/kg}$	$D_{CJ} = 6824.932\,\mathrm{m/s}$
Detonation Product Composition at C-J Point (Molar Basis)					
C_β	0.08826	H_2O	0.32308	NH_3	0.24990
N_2	0.13012	Al_2O_3(L)	0.17957	Al_2O_3	0.00103
Al_2O_3(a)	0.01067	Al_2O_2	0.00048	NO	0.00071
CO_2	0.00002	O_2	0.00002	CO	0.00001
H_2	0.01684				

Table 2. Values of mean free path of the gas and Knudsen number at the C-J point.

d_p **(nm)**	ℓ **(nm)**	***Kn***
0.3	0.069	0.01

Commonly, the kernel rate for systems whose dynamics fall within the continuum mechanics paradigm is given by [85]

$$\beta^l(v-u,u) = \frac{2k_BT}{3\mu}\left[\frac{1}{(v-u)^{1/3}} + \frac{1}{u^{1/3}}\right]\left[(v-u)^{1/3} + u^{1/3}\right], \tag{21}$$

where μ stands for the gas dynamic viscosity and k_B for the Boltzmann constant. The gas dynamic viscosity is estimated as

$$\mu = \frac{\ell \cdot \bar{c} \cdot \rho}{2}, \tag{22}$$

where $\bar{c}$ represents the average velocity of the gas molecules, defined as [129]

$$\bar{c} = \sqrt{\frac{3R_gT}{M_g}}, \tag{23}$$

with M_g denoting the molar mass of the gas and R_g the ideal gas constant.

To analyze the influence of the kernel on the PSD dynamics and extract useful insights for interpreting the results, we investigate the dependence of the kernel rate on the volume of the colliding particles. The values used to simulate the kernel rate are $\mu = 0.135\,44\,\text{cP}$, $\bar{c} = 2363.4\,\text{m/s}$, and $M_g = 19.5157\,\text{g/mol}$, with the temperature taken as T_{CJ} listed in Table 1. Figure 3 presents the results obtained for the collision frequency between a generic particle of fixed volume $1000\,\text{nm}^3$ and particles of different volumes u.

The kernel rate exhibits different behaviors depending on the volume of the colliding particles. For a given particle with volume $v - u$, the collision rate is higher when the volume u of the colliding particle is smaller, with the rate of decrease proportional to $u^{-\frac{1}{3}}$. Conversely, the kernel for collisions between particles of volume $v - u$ and larger particles u shows a considerably smoother increase than the decrease observed for smaller particles, with the rate of increase proportional to $u^{\frac{1}{3}}$. Additionally, the decrease in the difference between the volumes of the colliding particles leads to a minimum value of the kernel, occurring when the particles have identical volumes, with $\lim_{v-u\to u} \beta^l(v-u,u) = \frac{8k_BT}{3\mu}$.

The kernel trend shown in Figure 3 suggests a very rapid dynamics of the PSD, reaching a distribution close to its final state within a few microseconds. Additionally, this trend indicates a narrowing of the PSD range, as smaller particles will be "consumed" faster than larger ones.

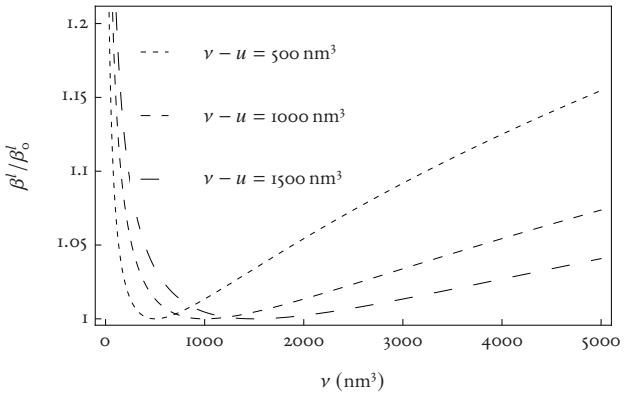

Figure 3. Normalized coalescence kernel for particle collisions with volumes of $500\,\text{nm}^3$, $1000\,\text{nm}^3$, and $1500\,\text{nm}^3$.

The coagulation kernel used to model the particle collision phenomenon is based on the frameworks proposed by Ree et al. [84] and Shaw and Johnson [130]. This kernel is designed for carbon particles generated by detonation operating under the Brownian regime. In this regime, the relative motion of two independent particles, with radii $\mathcal{R}_{v-u}$ and $\mathcal{R}_u$, is governed by diffusion with a combined diffusion coefficient $\mathcal{D}_{v-u,u} = \mathcal{D}_{v-u} + \mathcal{D}_u$, where $\mathcal{D}_{v-u}$ and $\mathcal{D}_u$ are the diffusion coefficients of the two particles. The collision frequency for the coagulation process is given by

$$\beta^g(v-u,u) = 4\pi\left(\mathcal{D}_{v-u} + \mathcal{D}_u\right)\cdot\left(\mathcal{R}_{v-u} + \mathcal{R}_u\right) \tag{24}$$

Using the Stokes–Einstein equation, which relates the diffusion coefficient $\mathcal{D}$ of a particle of radius $\mathcal{R}$ to the viscosity of the medium via $\mathcal{D} = \frac{k_BT}{6\pi\mu\mathcal{R}}$, the coagulation kernel simplifies to

$$\beta^g(v-u,u) = \frac{2k_BT}{3\mu}\left[\frac{1}{(v-u)^{1/3}} + \frac{1}{u^{1/3}}\right]\left[(v-u)^{1/3} + u^{1/3}\right] \tag{25}$$

Equation (25) resembles the coalescence kernel described by Equation (21). This similarity is consistent with the findings of Ramkrishna [126], as both coalescence and coagulation are aggregation processes that share a common mathematical representation, as given by Equation (21).

3.3. PBE Discretization

The numerical solution of the Population Balance Equation (PBE) is obtained by discretizing the spatial dimension using finite element or finite difference methods. This process transforms the continuous problem into a system of ordinary differential equations (ODEs), which are then solved using an implicit integrator. The number concentration of particles for each size class, referred to as a bin, is tracked throughout the simulation. Further details on this approach are discussed subsequently.

The accuracy of the discretization scheme is related to the mesh density: finer meshes yield more accurate results but also increase the size of the system of equations, which can lead to higher computational costs. Consequently, there is a trade-off between solution accuracy and computational effort. In particular, the choice of mesh size and node placement (especially in fixed-node strategies) must balance these two factors effectively.

To approximate a continuous property with distribution $F(x)$ using a discrete representation, two main paradigms are commonly employed [131]:

1. Interpolation method: The value of $F(x_i)$ is obtained by solving the Population Balance Equation (PBE) at discrete nodes x_i, where $i \in \{1, \ldots, K+1\}$, and the entire distribution is reconstructed using interpolation. Here, K represents the number of nodes.
2. Class averaging method: The value of $F(\vartheta_k)$ for $k \in \{1, \ldots, K\}$ is computed for discrete classes $[x_k, x_{k+1}]$, which are slices of the original distribution. In this method, ϑ_k is a representative point within $[x_k, x_{k+1}]$, and $F(\vartheta_k)$ is given by

$$F(\vartheta_k) = \frac{\int_{x_k}^{x_{k+1}} F(x) \cdot \mathrm{d}x}{x_{k+1} - x_k}.$$

Here, k denotes the bins.

Our approach utilizes the second paradigm, where the number concentration of particles in the bins is represented by values at predefined points, known as pivots. This method is commonly employed to ensure the conservation of the property $F(x)$ [127]. The effectiveness of the discretization method depends on the function space used for interpolation (if the first paradigm is applied) or the number of discrete classes (if the second paradigm is used).

Discretization methods for the PBE generally fall into two categories:

1. Fixed pivots: The location of bin points remains constant over time [127].
2. Moving pivots: The bin points are dynamically adjusted [128].

Alternative approaches, such as finite element and wavelet methods, are also documented (see Alvarez et al. [132], Chatzi and Kiparissides [133], Chen et al. [134], Gelbard and Seinfeld [135], Hounslow et al. [136], Kiparissides [137], Nicmanis and Hounslow [138], Singh and Ramkrishna [139,140]). While finite element methods address mass and volume conservation issues, they introduce higher complexity. Recently, moving grids have been successfully applied to solve Population Balance Equations (PBEs) [141–143]. Although these grids can adapt dynamically to follow the particle size distribution (PSD), their use in scenarios where particulate phenomena are coupled with other processes may encounter certain limitations.

In scenarios where the velocity of the particle size distribution (PSD) dynamics is significant, adaptive or moving mesh methods may offer better accuracy. Moving grids can better capture dynamic features by concentrating nodes in regions with steep gradients. However, applying moving-pivot methods, as proposed by Kumar and Ramkrishna [128] and Nopens and Vanrolleghem [144], presents numerical challenges when concentrations approach zero. This difficulty is particularly related to the equations governing pivot motion, which complicate the domain expansion. Conversely, although moving-pivot methods facilitate narrower meshes, they require solving additional ODEs for pivot motion, significantly increasing problem stiffness and computational time. Fixed-pivot methods,

while simpler and more interpretable, offer a clear trade-off between accuracy and computational effort. Consequently, we implemented a fixed-pivot method with a sufficiently refined mesh to ensure accurate results.

Applying the fixed-pivot framework to our problem enables us to discretize the continuous domain of particle volumes. We consider the domain $Y = [x_{\min}, x_{\max}]$, where the limits are chosen to capture the dynamics of the particle size distribution (PSD) within the time window of interest. This domain is divided into discrete classes of either constant or variable width, with the assumption that the number concentration of particles outside Y is negligible.

Let n_k denote the number concentration of particles in each volume class $[x_k, x_{k+1}]$. The volume of these classes, $[x_k, x_{k+1}]$, is assumed to be constant over time and is represented by the pivot value v_k, which is the midpoint of the class interval. The discretization of the Population Balance Equation (PBE) for modeling the particle size distribution (PSD) dynamics, considering only the coalescence phenomenon (i.e., Equation (18)), results in the following equation:

$$\frac{\mathrm{d}n_k}{\mathrm{d}t} = \frac{1}{2}\sum_{i=1}^{k-1} \beta^l(v_i, v_{k-i}) \cdot n_i \cdot n_{k-i} - n_k \cdot \left[\frac{2u_R}{R} + \sum_{i=1}^{K} \beta^l(v_i, v_k) \cdot n_i\right], \quad \forall k \tag{26a}$$

$$n_k(0) = n_k^0, \quad \forall k \tag{26b}$$

where all variables are defined as previously described, and n_k^0 represents the initial number concentration of particles at $t = 0$.

The accuracy of the numerical solution is highly dependent on the number of classes used to discretize the domain [126]. This choice involves a trade-off between result quality and computational effort; while very fine meshes can provide accurate solutions, they may also introduce numerical instability due to increased stiffness in the Jacobian matrix, leading to higher computational costs. Conversely, excessively narrow grids might fail to capture the essential features of the solution.

Another consideration is the dynamic nature of the solution, which can evolve spatially over time. Typically, large rates of change are observed initially for small particles, with high rates of change eventually developing for larger particles. This dynamic behavior can be addressed by using adaptive or moving mesh techniques or by refining a fixed mesh. To balance accuracy and computational efficiency, many approaches employ size classes in geometric progression, resulting in non-uniform meshes. This method improves accuracy for small particles at early time steps without the need for an overly fine mesh throughout. In this approach, the recurrence relation for meshing is

$$a_k = a_1\, r^k \tag{27}$$

where a_k denotes the amplitude of the kth class, a_1 represents the amplitude of the first bin, and r is the progression ratio determined by

$$\sqrt[3]{\frac{x_{\max}}{x_{\min}}} = \frac{r^k - 1}{r - 1} \tag{28}$$

This strategy allows for a more efficient mesh configuration while maintaining good accuracy for the initial and evolving stages of the solution.

The non-adaptivity of the mesh presents challenges when dealing with newly formed particles whose sizes do not exactly match any of the fixed pivots. In these cases, the newly formed particles are redistributed to adjacent pivots to ensure the conservation of two arbitrary moments of the distribution. The fixed-pivot discretization scheme uses a

redistribution algorithm mathematically represented by an operator that simultaneously conserves both mass and particle number. This operator is defined as [86]

$$\chi_{i,j,k} = \begin{cases} \frac{\nu_{k+1}-(\nu_i+\nu_j)}{\nu_{k+1}-\nu_k} & \text{if} \quad \nu_k \leq \nu_i+\nu_j \leq \nu_{k+1} \\ \frac{(\nu_i+\nu_j)-\nu_k}{\nu_k-\nu_{k-1}} & \text{if} \quad \nu_{k-1} \leq \nu_i+\nu_j \leq \nu_k \\ 0 & \text{otherwise} \end{cases} \tag{29}$$

Equation (29) specifies the weights used to redistribute newly formed droplets resulting from the coalescence or coagulation of particles with volumes corresponding to pivots i and j to the pivot of class k. The redistribution occurs under the constraint $\nu_{k-1} \leq \nu_i + \nu_j \leq \nu_{k+1}$. The majority of the particles are assigned to the pivot closest to the sum $\nu_i + \nu_j$, with a proportionally smaller fraction assigned to the adjacent pivot further away. This operator assumes that within each class of discrete entities, the concentration is linearly approximated, and the pivot serves as a representative average for the class.

The reformulation of Equation (26) to include the redistribution operator $\chi_{i,j,k}$ yields

$$\frac{\mathrm{d}n_k}{\mathrm{d}t} = \sum_{i=1}^{k} \Delta_{i,k-i,k} \cdot \chi_{i,k-i,k} \cdot \beta^l(\nu_i, \nu_{k-i}) \cdot n_i \cdot n_{k-i} - n_k \cdot \left[\frac{2u_R}{R} + \sum_{i=1}^{K} \beta^l(\nu_i, \nu_k) \cdot n_i \right], \quad \forall k \tag{30a}$$

$$n_k(0) = n_k^0, \quad \forall k \tag{30b}$$

where

$$\Delta_{i,j,k} = \begin{cases} 1/2 & \text{if } i = j, \\ 1 & \text{if } i \neq j \end{cases}.$$

When extending this approach to discretize the PBE for both coalescence and coagulation phenomena, we obtain

$$\begin{aligned} \frac{\mathrm{d}n_k}{\mathrm{d}t} = & \sum_{i=1}^{k} \Delta_{i,k-i,k} \cdot \chi_{i,k-i,k} \cdot \beta^l(\nu_i, \nu_{k-i}) \cdot n_i \cdot n_{k-i} + \sum_{i=1}^{k} \Delta_{i,k-i,k} \cdot \chi_{i,k-i,k} \cdot \beta^g(\nu_i, \nu_{k-i}) \cdot n_i \cdot n_{k-i} - \\ & - n_k \cdot \left[\frac{2u_R}{R} + \sum_{i=1}^{K} \beta^l(\nu_i, \nu_k) \cdot n_i + \sum_{i=1}^{K} \beta^g(\nu_i, \nu_k) \cdot n_i \right], \quad \forall k \end{aligned} \tag{31a}$$

$$n_k(0) = n_k^0, \quad \forall k \tag{31b}$$

Here, the operator Δ is defined as in Equation (30a), and $\beta^l(\nu_i, \nu_j)$ and $\beta^g(\nu_i, \nu_j)$ are given by Equation (25).

3.4. Initial Particle Size Distribution

The numerical solution of the PBE describing PSD dynamics, as formulated in Equation (19), requires the specification of the initial distribution $n^0(\nu)$. Due to the complexity of the process used in the formation of alumina particles and the time window during which particulate phenomena occur, accurately estimating the initial distribution is challenging. To address this, we assume that the initial mass distribution of alumina over the particle size domain follows a log-normal distribution. This assumption is supported by the general forms proposed by Friedlander [85] to describe the size of particles formed through condensation. Additionally, empirical evidence from controlled experiments further validates this assumption, as the final PSD of nanoparticles across a wide range of materials often exhibits a log-normal distribution.

Given that growth and nucleation terms are negligible, the initial PSD is expected to be log-normal, with coalescence and coagulation shifting the mean towards larger volumes

and increasing variability. Log-normal distributions are characterized by longer tails at larger sizes and can be mathematically expressed as

$$f(\nu) = \frac{N_\infty}{\sqrt{2\pi}\,\nu\,\ln(\sigma_g)} \exp\left\{-\frac{\left[\ln(\nu) - \ln(\nu_g)\right]^2}{2\ln^2(\sigma_g)}\right\}, \tag{32}$$

where N_∞ is the total value of the approximated property, $\ln(\nu_g) = \int_0^\infty \ln[n(\nu)\cdot\nu]\,\mathrm{d}\nu$ is the logarithmic volume average, $\ln^2(\sigma_g) = \int_0^\infty \ln\left[n(\nu)\cdot(\nu-\nu_g)^2\right]\mathrm{d}\nu$ is the logarithmic volume variance, and σ_g is the standard deviation.

If a mass-based PSD is to be computed, N_∞ represents the total mass of alumina theoretically formed (available at the C-J point), denoted as $m_{Al_2O_3}(0)$. This leads to

$$m_{Al_2O_3,k}(0) = \frac{m_{Al_2O_3}(0)}{\sqrt{2\pi}\,\nu_k\,\ln(\sigma_g)} \exp\left\{-\frac{\left[\ln(\nu_k) - \ln(\nu_g)\right]^2}{2\ln^2(\sigma_g)}\right\}, \tag{33}$$

where $m_{Al_2O_3,k}(0)$ represents the mass frequency corresponding to the k^{th} class of volume.

The logarithmic mean considered in Equation (32) corresponds to the critical diameter of the nuclei formed at the C-J point, as determined by the Kelvin–Gibbs relation (see Equation (1)). This assumption is crucial for reinforcing some of the model considerations presented in Section 2. Specifically, the critical diameter pertains to nuclei that have already condensed into metallic liquid droplets, implying that the formation of additional stable entities during the expansion of the detonation matrix is neglected. Consequently, after the C-J point, the system is treated as a gaseous phase with liquid droplets immersed within it, where these droplets collide with each other. This approach assumes no further nucleation of new entities, as the saturation ratio significantly decreases due to the rapid drop in temperature and pressure.

The standard deviation of the initial PSD is chosen such that 99.7 % of the droplets formed at the C-J point are accounted for. Since only liquid alumina droplets are considered, the total mass of particles at C-J point is determined based on the dimensions of the explosive matrix, as previously described, and data obtained from a simulation using `THOR` (as shown in Table 1). The results in Table 3 provide the additional parameters necessary to determine the initial mass distribution.

Table 3. Parameters involved in the determination of the initial PSD.

$m_{Al_2O_3}(0)\,(\mathbf{kg})$	$\nu_g\,(\mathbf{nm}^3)$	$\sigma_g\,(\mathbf{nm}^3)$
0.0392	155	51.8

The initial particle number concentration required by Equation (19) is derived from $m_{Al_2O_3}(0)$ as follows:

$$n_k(0) = \frac{m_{Al_2O_3}(0)}{\rho_{Al_2O_3(0)}\,\nu_k\,V(0)}, \quad k \in \{1,\cdots,K\}, \tag{34}$$

where $\rho_{Al_2O_3}(0)$ is the density of liquid alumina and $V(0)$ is the volume of the expanding system at C-J point.

3.5. Time Integration

The model describing gas expansion beyond the C-J point, represented by Equations (3), (6)–(10), (12a)–(12c), (12e)–(12g), (13) and (14), is solved concurrently with the discretized form of the PBE modeling the PSD dynamics. This includes Equations (20)–(23) and (30a) if only coalescence phenomena are considered or Equations (20)–(23), (25) and (31) when both coalescence and coagulation phenomena are considered.

The vector $\mathbf{y}^d \equiv (u_R, \rho, V, R, p, p_\kappa, p_{\kappa 1}, p_{\kappa 2}, e, e_\kappa, e_{\kappa 1}, e_{\kappa 2}, T, T_{sol})$ encompasses the variables involved in the detonation process model. Initial conditions for $\mathbf{y}^d$ are provided by Equation (4) for radial expansion velocity and in Table 1 for all other variables. Similarly, $\mathbf{y}^p \equiv (\beta_{i,j}, \mu, \bar{c}, \ell, n_k)$, $\forall i, j, k \in \{1, \cdots, K\}$ contains the variables describing the PSD dynamics, with initial conditions for n_k, $\forall k$, presented in Section 3.4. The combined vector $\mathbf{y} \equiv (\mathbf{y}^d | \mathbf{y}^p)^\intercal$ aggregates all variables.

The *Mathematica 10* platform was used to integrate the Differential-Algebraic Equations (DAEs) system described above [145]. The IDA solver, which is a variable-order, variable-coefficient Backward Differentiation Formula (BDF) algorithm, was employed to handle the DAE system. IDA operates in a fixed-leading-coefficient form, with the order varying between 1 and 5, and is capable of solving systems of the form $F\left(\frac{\mathrm{d}\mathbf{y}}{\mathrm{d}t}, \mathbf{y}, t\right) = 0$ [146]. The solution of the resulting non-linear system is achieved using a variant of the Newton algorithm, and interpolation is employed to compute solutions at time points other than those iterated by the integrator.

4. Results

This section presents the simulation results for the physical system mathematically described in the previous sections. To facilitate the analysis, key conclusions are presented and discussed concurrently. Although the numerical simulation approach involves solving the equations for both the detonation of the emulsion matrix and the particulate transformations simultaneously, the characteristics of each phenomenon are analyzed separately in the following two subsections.

4.1. Detonation Results

In Section 2, it was noted that closing the system of equations governing detonation dynamics requires an Equation of State (EoS). In this study, the Mie-Grüneisen EoS is employed, with the cold curve described by the JWL (Jones–Wilkins–Lee) EoS, which depends on five parameters (A, B, R_1, R_2, ω) characteristic of the explosive family used. Table 4 lists the JWL EoS parameters specific to the ANFO explosives family utilized in this work, sourced from the literature [115]. Additionally, the parameter κ, derived from the conditions at the C-J point using Equation (12d) and the properties listed in Table 4, is also included. Table 5 presents the parameters relevant to determining the dynamics of radial expansion velocity, which were predicted through simulations using the thermochemical code `THOR` [147].

Table 4. JWL EoS parameters.

Parameter	Value	Parameter	Value	Parameter	Value
A	12.5×10^9 Pa	B	1.891×10^9 Pa	R_1	3.907
R_2	1.118	ω	0.57	κ	1.983×10^9 Pa

Table 5. Parameters employed in the radial expansion velocity determination.

Parameter	Value	Parameter	Value	Parameter	Value
D_{CJ}	6825 m/s	u_{CJ}	1747 m/s	R_{CJ}	0.0217 m
R_0	0.025 m	θ	0.349 066 rad	R_c	0.0687 m/s
$u_R(0)$	1604 m/s				

The dynamics of the detonation process are illustrated in Figure 4. Figure 4a displays the expansion velocity of the system, which corresponds to a rapid decline in pressure. Notably, the rate of this decline is not constant over time; it exhibits larger initial derivatives and eventually stabilizes as the system temperature approaches the solidification point of alumina. This behavior is consistent with the physical principles governing detonation phenomena and is supported by various literature sources, such as Arienti et al. [148].

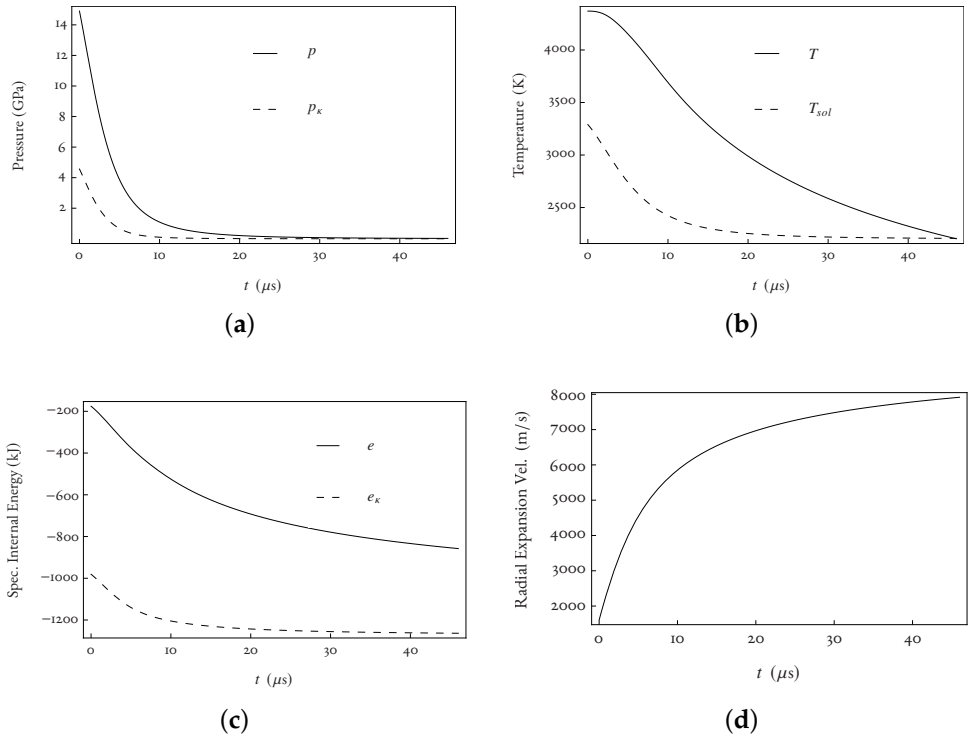

Figure 4. Dynamics of key properties during the expansion of the detonation matrix: (**a**) isentropic vs. system pressure; (**b**) system temperature vs. solidification temperature of liquid alumina particles; (**c**) isentropic vs. system internal energy; (**d**) radial expansion velocity.

In Figure 4b, the system temperature is shown to decrease during expansion. A comparison between the pressure and temperature dynamics reveals that the temperature exhibits a much smoother evolution than the pressure, a trend consistent with established references [117]. This behavior aligns with the typical differences in propagation speeds between pressure and temperature waves in chemical and mechanical systems. Additionally, Figure 4b illustrates the relationship between the solidification temperature of alumina particles and the system pressure. As the expansion progresses, both the solidification temperature and the pressure decrease, following a similar profile.

Moreover, Figure 4b indicates that the time window for particle growth lasts only about 46 µs, a relatively short duration compared to other gas-to-solid nanoparticle production methods. Since the dynamics of temperature are heavily influenced by pressure, and pressure itself is governed by the "cold curve", the parameters of the JWL EoS are critical for ensuring the accuracy of the final results. Figure 4c shows the trends in specific internal energy. Given that total enthalpy is assumed constant, with thermal energy converting into kinetic energy, the internal energy profile closely mirrors the temperature trend.

Figure 4a,c also highlight the differences between the curves for system pressure and internal energy and their corresponding isentropic reference states. In light of Equations (11)–(13), it is evident that the observed decrease in temperature during expansion is directly correlated with the diminishing gap between the system pressure and internal energy curves and their respective isentropic counterparts.

Figure 4d illustrates the dynamics of radial expansion velocity, which is directly related to the expansion volume. The observed trend is consistent with findings from other studies [149,150]. Initially, the radial expansion velocity increases rapidly, followed by a phase where it asymptotically approaches a maximum value as the system pressure nears atmospheric levels. However, our results show higher velocities than those typically reported in the literature. Several factors may contribute to this discrepancy. First, the theoretical basis for the ordinary differential equation (ODE) describing radial expansion velocity was originally derived for central flow lines. In this study, it was extended to repre-

sent the radial expansion of all infinitesimal layers independent of their position and time. Second, Lu [151] observed lower velocities using a similar ODE to Equation (8) but with an additional empirical term proportional to the square of the velocity, which decelerates expansion. This term was omitted in our model to maintain system independence and exclude specific features of the detonation matrix and chamber. As a result, the exclusion of this term may lead to higher expansion velocities and affect the time required to reach the solidification temperature. The impact of this potential discrepancy on particulate phenomena will be analyzed in the subsequent subsection.

Finally, the estimate for the initial radial expansion velocity (at the C-J point) relies on parameters such as the curvature radius and detonation velocity angle θ, which were determined experimentally for a range of high-purity detonation matrices. Given that our matrix is a non-pure emulsion, these parameters may involve some inaccuracies. Additionally, the expansion velocity is dependent on the system pressure and, consequently, on the parameters of the JWL EoS.

4.2. Particulate Dynamics

The accuracy of the mesh used to describe the initial particle size distribution (PSD), as determined by the strategy outlined in Section 3.4, is first assessed. The mesh domain is configured to minimize errors associated with the formation of larger particles, which can result in mass loss during the simulation process. The mesh was established by defining the minimum and maximum volumes that bound the domain Y and specifying the number of classes to be used. The pivots for the mesh were determined using Equations (27) and (28). The parameters used are summarized in Table 6. In practice, the grid was configured by adjusting the progression ratio r to balance the accuracy of the time-varying PSD representation with computational efficiency. The grid defined in Table 6 ensures that the squared error between the PSD calculated with 101 nodes and a grid of twice the density remains below 1 %.

Table 6. Parameters used in the determination of the mesh.

$x_{\min}$ (nm^3)	$x_{\max}$ (nm^3)	$a_1(\mathrm{nm}^3)$	K ( )
0	$9.548\,34 \times 10^{10}$	$5.235\,99 \times 10^{-4}$	70

Figure 5a shows the initial mass distribution of liquid alumina in both continuous and discretized domains, determined using Equation (33) with the moments listed in Table 3. The geometric scale employed effectively captures the features of the continuous initial PSD. Figure 5b presents the corresponding number concentration PSD, derived using Equation (34).

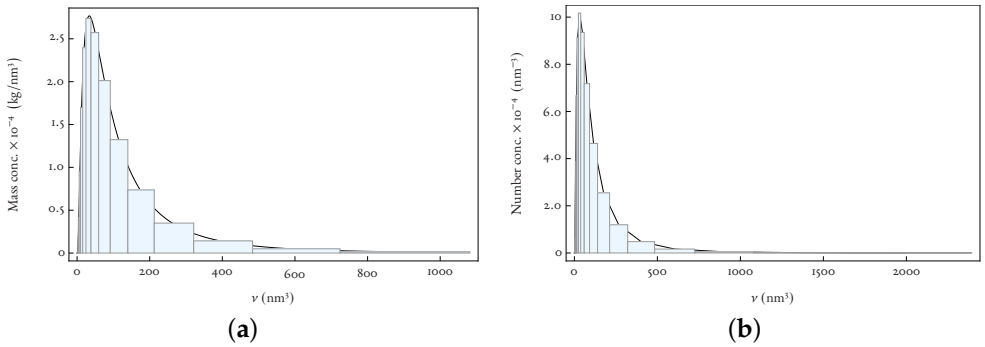

Figure 5. Initial numerical concentration distributions of liquid alumina particles: (**a**) mass-based PSD; (**b**) number concentration-based PSD.

Figure 6 illustrates the dynamics of mass and number concentration of liquid alumina particles from the C-J point to solidification, assuming only coalescence phenomena.

The results align closely with predictions from Section 2 and with observations from gas-to-solid alumina growth studies [86]. The data highlight the critical role of the first few microseconds in shaping the process, with the PSD rapidly shifting towards larger particle sizes and stabilizing.

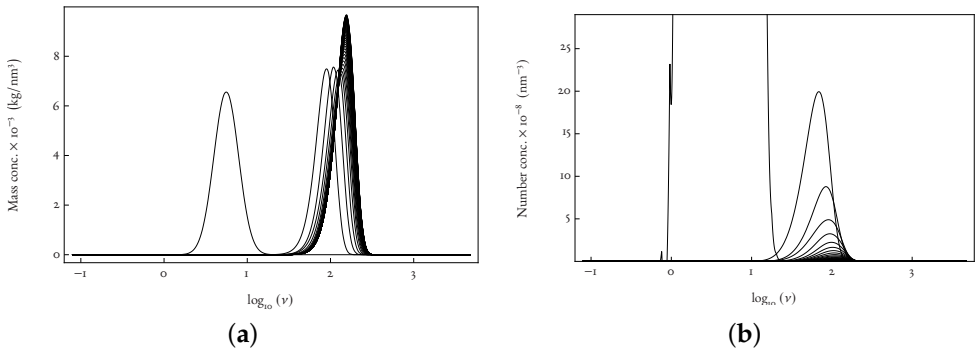

(**a**) (**b**)

Figure 6. Evolution of the particle size distribution: (**a**) mass-based PSD; (**b**) number concentration-based PSD.

Several factors influence this behavior. Firstly, the high collision frequency under the initial thermodynamic conditions results in a rapid evolution of the PSD. Figure 7 shows that both the coalescence kernel, in Figure 7a, and the total particle number, in Figure 7b, exhibit significant changes shortly after crossing the C-J point. Mathematically, the system of ODEs has large negative eigenvalues at $t = 0$, driving the system towards a near-steady state within a few microseconds. As time progresses, the magnitude of these eigenvalues decreases, leading to minor changes in the pivot dynamics.

Secondly, the expansion effect reduces collision frequency as the volume expands, leading to rarification. This effect is significant in the PBE due to the high expansion rate, denoted by $\frac{2\,u_R}{R}$. Additionally, the first microseconds have a substantial impact on particle size, with large particles forming from the collision of smaller ones, contributing to rarification. This is explained by the varying coalescence kernels for small versus large particles, as shown in Figure 3.

Figure 6a further reveals that the mass-based PSD tightens as smaller particles coalesce into larger ones, with a slow shift towards larger particle sizes and increased PSD height due to constant overall mass. The number concentration-based PSD also shows a gradual increase in average particle size with a decrease in overall concentration, reflecting the expansion of the detonation matrix and resulting rarification.

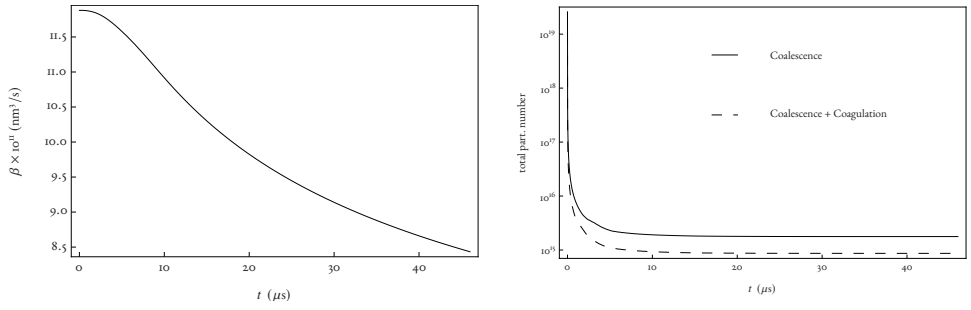

(**a**) (**b**)

Figure 7. Dynamics of (**a**) coalescence kernel for two isolated particles, each with a fixed volume of 2.7488 nm^3, and (**b**) total number of liquid alumina particles.

To simplify the analysis of process velocity, we define the ratio of the number of particles at time t relative to another time t_1, denoted as $\eta(t, t_1)$, by the following equation:

$$\eta(t, t_1) = \frac{\sum_{k=1}^{K} n_k(t)}{\sum_{k=1}^{K} n_k(t_1)} \tag{35}$$

The ratio $\eta(1\,\mu s, 0\,\mu s)$ is nearly equal to $\eta(46\,\mu s, 1\,\mu s)$, highlighting the significant impact of the initial moments on the final characteristics of the product. Additionally, Figure 8a demonstrates that by $t = 1\,\mu s$, 58.4 % of the total observed increase in average particle diameter has already occurred (see Table 7).

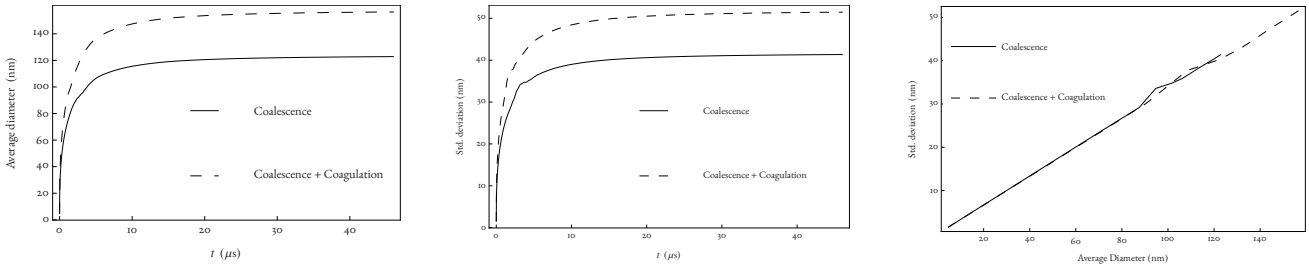

(**a**) (**b**) (**c**)

Figure 8. Evolution of particle size characteristics: (**a**) Aaverage particle diameter distribution under coalescence-only and coalescence+coagulation conditions; (**b**) standard deviation of the particle diameter distribution; (**c**) relationship between the standard deviation and the average particle diameter.

Table 7. Metrics of the PSD at different time instants.

Measure	**Coal**			**Coal + Coag**		
	$t = 0\,\mu s$	$t = 1\,\mu s$	$t = 46\,\mu s$	$t = 0\,\mu s$	$t = 1\,\mu s$	$t = 46\,\mu s$
Particles' number	2.57×10^{20}	7.62×10^{16}	1.77×10^{16}	2.57×10^{20}	3.78×10^{16}	8.66×10^{15}
Average diameter (nm)	6.67	71.53	122.84	6.67	90.36	156.47

Coal—coalescence phenomena; Coal + Coag—coalescence + coagulation phenomena.

Figure 8a shows the evolution of the average particle diameter and standard deviation throughout the simulation, considering both coalescence alone and the combined effects of coalescence and coagulation. The rapid early changes in the particle size distribution are evident. When only coalescence is considered, the most representative diameter by the end of the simulation corresponds to a pivot of 121.992 nm, with a volume of $9.505\,99 \times 10^5$ nm^3. When both coalescence and coagulation are included, the representative diameter shifts to 157.127 nm, corresponding to a volume of $2.031\,21 \times 10^6$ nm^3.

The standard deviation, as depicted in Figure 8b, progressively increases throughout the simulation, closely reflecting the behavior of the average diameter. The coefficient of variation (C_v), a crucial metric for assessing PSD dispersion, exhibits a linear increase in both scenarios (see Figure 8c), reinforcing the log-normality of the PSD [152]. In the coalescence-only scenario, C_v stabilizes at approximately 0.34, while in the combined scenario, it remains around 0.33, with both values showing minimal fluctuation. This consistency, which mirrors the initial distribution, suggests that the particle distribution is largely preserved, with only the mean and standard deviation increasing over time as a result of coagulation and coalescence phenomena. Minor deviations observed at larger diameters may be attributable to numerical inaccuracies.

In Section 3, we made assumptions to select the most appropriate kernel based on the particles' motion regime. The validity of this assumption throughout the simulation period is assessed in Figure 9. The Knudsen number's dynamic behavior reveals that it only exceeds 0.1 near the end of the simulation, confirming our initial assumption. Furthermore,

during this late stage, particle growth is nearly negligible, and the rise in the Knudsen number is primarily due to the increased mean free path, which results from the decreasing density of the expanding matrix.

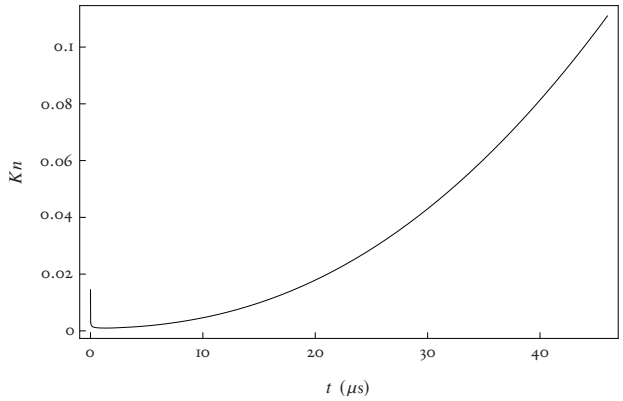

Figure 9. Evolution of the Knudsen number throughout the simulation.

4.3. Model Verification and Validation

The primary goal of this work was to provide a foundation of phenomenological knowledge to assist industrial producers of nanoparticles via detonation processes in optimizing their production methods. The model reveals two key trends: (i) the most critical phases for controlling PSD size occur within the first µs; and (ii) the only feasible approach to influencing PSD size is through adjusting the energy released from the detonation matrix, which requires careful selection, especially in terms of matrix formulations.

For model verification, we varied kernel parameters, finding that they have only a limited impact on PSD until solidification. To compare the model's PSD predictions with experimental results, we conducted experiments in a controlled chamber. While simulations tend to underestimate the PSD, microscopic images suggest that an improved disaggregation technique is needed to reduce particle coalescence, as some coalescence remains visible even after washing.

Another noteworthy aspect is that our detonation model, which incorporates simplified assumptions for numerical feasibility, slightly overestimates the radial velocity of the detonation wave. This discrepancy stems from assuming that each infinitesimal cylindrical layer progresses uniformly at a rate based on the velocity of the outer layer, grounded in the assumption of homogeneity within the detonation matrix in the gas phase. Other thermochemical codes suggest that the actual radial velocity is 10 % to 30 % lower. Despite this, the difference has minimal effect on particle size, as a lower radial velocity only slightly prolongs the time to particle solidification, leading to a marginal increase in average diameter. This effect remains minor because of the following: (i) the extension in solidification time is less than 5 µs; and (ii) the increase in average diameter becomes negligible after 20 µs. Consequently, any additional time beyond 20 µs has minimal impact on PSD.

Improving the model's predictive accuracy could involve introducing heterogeneity in matrix dynamics. However, this approach poses numerical challenges, as it requires solving a distinct Population Balance Equation (PBE) at each radially evolving position through discretization. Another potential approach is to integrate the simulation tool with a thermochemical code, enabling more accurate and straightforward characterization of the Chapman–Jouguet point. Additionally, integration with a general-purpose finite element analysis tool could allow for precise detonation simulations, generating data files that the PBE solver can subsequently use to dynamically simulate the particulate phenomena.

5. Conclusions and Future Work

Detonation is emerging as a promising method for producing metallic oxide nanoparticles, sharing key features with other gas-to-solid techniques. Its theoretical potential is significant due to the high energy involved, which can fully vaporize metallic species and facilitate oxidation in the gas phase. However, industrial adoption faces challenges. Knowledge gaps often arise concerning the complex phenomena of matrix detonation and the impact of intensive variables on particle formation and growth. Additionally, controlling the process remains difficult, potentially limiting its industrial use.

This paper aims to address these knowledge gaps by presenting a phenomenological tool for prediction purposes. To our knowledge, there are no existing models in the literature that use first principles to address nanoparticle production via detonation. Our tool, combining theoretical formulations with robust numerical algorithms, is designed to forecast and extract knowledge about this process.

The developed conceptual tool consists of two models: one describing the detonation of an emulsified matrix containing explosive material and another representing particulate phenomena. These models are solved numerically, considering the extensive and intensive properties affecting particle dynamics. While the detonation model uses approximate methods to balance computational efficiency with capturing main trends, it incorporates a thermochemical code to compute "jump conditions" based on the Chapman–Jouguet theory. These conditions are then used to model the radial expansion of the gas phase post-detonation, represented by concentric rings with radial and axial homogeneity. The axial expansion is treated as infinitesimally thin elements expanding radially, all following similar thermodynamic trajectories with minimal time delays. The Mie-Grüneisen Equation of State is used to describe the detonation products' thermodynamics, while the JWL EoS serves as the reference "cold curve".

The particulate dynamics are modeled using a Population Balance Equation (PBE) that accounts for both coalescence and coagulation. The initial particle size distribution (PSD) is assumed to be log-normal, with the average diameter derived from the Kelvin–Gibbs relation. Particle collisions are described using kernels for Brownian motion, and growth occurs via coalescence and coagulation until the matrix temperature reaches the solidification point of the metallic oxides. New nucleation during this period is not considered. The PBE is discretized using a fixed-pivot approach, leading to a set of Differential-Algebraic Equations (DAEs) representing particle number concentration.

The DAEs for detonation and PSD dynamics are solved with an implicit DAE solver over time. This approach is applied to predict the PSD of alumina nanoparticles produced from an ANFO aluminized matrix. Results align well with literature values, showing that particulate phenomena occur within a very short time window (5×10^{-5} s). Notably, the initial moments are crucial for PSD characteristics due to the rarefaction effect and rapid particle coalescence. For instance, 58.4 % of the average particle size increase occurs within the first microsecond. The PSD evolves towards larger particles, stabilizing in a few microseconds while maintaining a log-normal distribution.

The findings underscore the need for further sensitivity analysis of PSD parameters and process variables for optimization. Control challenges arise from the brief critical time window and limited controllability of the process. However, optimization can be achieved by selecting appropriate explosive materials and designing the explosive matrix. Future work will focus on optimizing these variables using the developed model and exploring additional knowledge related to detonation-based production and gas-to-solid strategies.

Author Contributions: Conceptualization: P.M.S.S., B.P.M.D., N.M.C.O. and J.L.S.A.C.; Methodology: P.M.S.S., B.P.M.D., N.M.C.O. and J.L.S.A.C.; Software: P.M.S.S.; Formal Analysis: B.P.M.D., N.M.C.O., J.L.S.A.C., R.A.L.M. and J.M.C.S.; Investigation: P.M.S.S., B.P.M.D., N.M.C.O., J.L.S.A.C., R.A.L.M.; Resources: N.M.C.O. and J.L.S.A.C.; Data Curation: P.M.S.S.; Writing—original draft preparation: P.M.S.S. and B.P.M.D.; Writing—review and editing: P.M.S.S., B.P.M.D., N.M.C.O., J.L.S.A.C., R.A.L.M. and J.M.C.S.; Supervision: N.M.C.O. and J.L.S.A.C.; Project administration: N.M.C.O. and J.L.S.A.C. All authors have read and agreed to the published version of the manuscript.

Funding: P.M.S.S. was supported by a grant from the FCT under project number PTDC/EQU-EPR/114990/2009.

Data Availability Statement: The software resources generated are proprietary.

Conflicts of Interest: J.M.C.S. was employed by the company Lifthium Energy. The remaining authors declare that the research was conducted in the absence of any commercial or financial relationships that could be construed as a potential conflict of interest.

References

1. Hawa, T.; Zachariah, M.R. Development of a phenomenological scaling law for fractal aggregate sintering from molecular dynamics simulation. *J. Aerosol Sci.* **2007**, *38*, 793–806. [CrossRef]
2. Gutsch, A.; Kramer, M.; Michael, G.; Muhlenweg, H.; Pridohl, M.; Zimmermann, G. Gas-phase production of nanoparticles. *Kona* **2002**, *20*, 24–37. [CrossRef]
3. Wei, C.; Zhang, Y.; Guo, J.; Han, B.; Yang, X.; Yuan, J. Effects of silica nanoparticles on growth and photosynthetic pigment contents of *Scenedesmus obliquus*. *J. Environ. Sci.* **2010**, *22*, 155–160. [CrossRef]
4. Skotland, T.; Iversen, T.; Sandvig, K. New metal-based nanoparticles for intravenous use: Requirements for clinical success with focus on medical imaging. *Nanomed. Nanotechnol. Biol. Med.* **2010**, *6*, 730–737. [CrossRef]
5. Abanades, S.; Chambon, M. CO_2 dissociation and upgrading from two-step solar thermochemical processes based on ZnO/Zn and SnO_2/SnO redox pairs. *Energy Fuels* **2010**, *24*, 2805–2822. [CrossRef]
6. Ganapathy, V.; Karunagaran, B.; Rhee, S. Improved performance of dye-sensitized solar cells with TiO_2/alumina core–shell formation using atomic layer deposition. *J. Power Sources* **2010**, *195*, 5138–5143. [CrossRef]
7. Glenn, J. Nanotechnology: Future military environmental health considerations. *Technol. Forecast. Soc. Chang.* **2006**, *73*, 128–137. [CrossRef]
8. Zheng, L.; Li, S.; Burke, P.J. Self-assembled gold nanowires from nanoparticles: An electronic route towards DNA nanosensors. In Proceedings of the Nanoengineering: Fabrication, Properties, Optics, and Devices, Denver, CO, USA, 2–6 August 2004; Volume 5515, pp. 117–124. [CrossRef]
9. Murray, C.B.; Norris, D.J.; Bawendi, M.G. Synthesis and characterization of nearly monodisperse CdE (E = sulfur, selenium, tellurium) semiconductor nanocrystallites. *J. Am. Chem. Soc.* **1993**, *115*, 8706–8715. [CrossRef]
10. Kung, H.H.; Ko, E.I. Preparation of oxide catalysts and catalyst supports: A review of recent advances. *Chem. Eng. J. Biochem. Eng. J.* **1996**, *64*, 203–214. [CrossRef]
11. Brinker, C.J.; Scherer, G.W. *Sol-Gel Science: The Physics and Chemistry of Sol-Gel Processing*; Academic Press: Boston, MA, USA, 1990.
12. Klein, L. *Sol-Gel Optics: Processing and Applications*; Kluwer Academic Publishers: Boston, MA, USA, 1994.
13. Corriu, R. *Molecular Chemistry of Sol-Gel Derived Nanomaterials*; Wiley: Chichester, UK, 2009.
14. Suslick, K.S.; Hyeon, T.; Fang, M. Nanostructured materials generated by high-intensity ultrasound: Sonochemical synthesis and catalytic studies. *Chem. Mater.* **1996**, *8*, 2172–2179. [CrossRef]
15. Sunstrom IV, J.E.; Moser, W.R.; Marshik-Guerts, B. General route to nanocrystalline oxides by hydrodynamic cavitation. *Chem. Mater.* **1996**, *8*, 2061–2067. [CrossRef]
16. Kishida, M.; Fujita, T.; Umakoshi, K.; Ishiyama, J.; Nagata, H.; Wakabayashi, K. Novel preparation of metal-supported catalysts by colloidal microparticles in a water-in-oil microemulsion; catalytic hydrogenation of carbon dioxide. *J. Am. Chem. Soc. Chem. Commun.* **1995**, *91*, 763–764. [CrossRef]
17. Kortan, A.R.; Hull, R.; Opila, R.L.; Bawendi, M.G.; Steigerwald, M.L.; Carroll, P.J.; Brus, L.E. Nucleation and growth of cadmium selenide on zinc sulfide quantum crystallite seeds, and vice versa, in inverse micelle media. *J. Am. Chem. Soc.* **1990**, *112*, 1327–1332. [CrossRef]
18. Pileni, M.P.; Motte, L.; Petit, C. Synthesis of cadmium sulfide in situ in reverse micelles: Influence of the preparation modes on size, polydispersity, and photochemical reactions. *Chem. Mater.* **1992**, *4*, 338–345. [CrossRef]
19. Pillai, V.; Kumar, P.; Hou, M.J.; Ayyub, P.; Shah, D.O. Preparation of nanoparticles of silver-halides superconductors and magnetic-materials using water-in-oil microemulsions as nano-reactors. *Adv. Colloid Interface Sci.* **1995**, *55*, 241–269. [CrossRef]
20. Arriagada, F.J.; Osseo-Asave, K. Synthesis of nanosize silica in aerosol OT reverse microemulsions. *J. Colloid Interface Sci.* **1995**, *170*, 8–17. [CrossRef]
21. Hopwood, J.; Mann, S. Synthesis of barium sulfate nanoparticles and nanofilaments in reverse micelles and microemulsions. *Chem. Mater.* **1997**, *9*, 1819–1828. [CrossRef]
22. Higgins, R.J.; Goldsmith, R.I. Process and System for Production of Organic Nanoparticles. U.S. 5879715, 9 March 1999.
23. Leslie-Pelecky, D.L.; Reike, R.D. Magnetic properties of nanostructured materials. *Chem. Mater.* **1996**, *8*, 1770–1783. [CrossRef]
24. Ying, J.Y.; Sun, T. Research needs assessment on nanostructured catalysts. *J. Electroceram.* **1997**, *1*, 219–238. [CrossRef]
25. Koch, C.C. Materials synthesis by mechanical alloying. *Annu. Rev. Mater. Sci.* **1989**, *19*, 121–143. [CrossRef]
26. Hu, E.L.; Shaw, D.T. Synthesis and Assembly. *In Proceedings of the WTEC Panel Report on Nanostructure Science and Technology: R&D Status and Trends in Nanoparticles, Nanostructured Materials, and Nanodevices*; Siegel, R.W., Roco, M.C., Eds.; World Technology Evaluation Center (WTEC): Washington, DC, USA, 1998; pp. 15–34.
27. Gleiter, H. Nanocrystalline materials. *Prog. Mater. Science* **1989**, *33*, 223–315. [CrossRef]

28. Siegel, R.W. Cluster-Assembled nanophase materials. *Annu. Rev. Mater. Sci.* **1991**, *21*, 559–578. [CrossRef]
29. Siegel, R.W. Nanophase Materials: Synthesis, Structure, and Properties. In Proceedings of the International Conference on the Physics of New Materials, Berlin, Germany, 29 August–2 September 1994; Volume 27, pp. 65–105. [CrossRef]
30. Riemenschneider, H.; Gutsch, A. Nanotechnology at Degussa—From Ideas to Actual Business. In Proceedings of the 2006 AIChE Annual Meeting CD-ROM Proceedings, San Francisco, CA, USA, 12–17 November 2006.
31. Rao, N.; Girshick, S.; Heberlein, J.; McMurry, P. Nanoparticle formation using a plasma expansion process. *Plasma Chem. Plasma Process.* **1995**, *15*, 581–606. [CrossRef]
32. Rosner, D.E. Flame synthesis of valuable nanoparticles: Recent progress/current needs in areas of rate laws, population dynamics, and characterization. *Ind. Eng. Chem. Res.* **2005**, *44*, 6045–6055. [CrossRef]
33. Zhao, T.; Wang, X.; Li, X.; Wang, Y.; Song, X.; Yan, H. Gaseous detonation synthesis of CoC nanoparticles/CNTs materials. *Mater. Lett.* **2019**, *236*, 179–182. [CrossRef]
34. Uyeda, R. Studies of ultrafine particles in Japan: Crystallography. Methods of preparation and technological applications. *Prog. Mater. Sci.* **1991**, *35*, 1–96. [CrossRef]
35. Friedlander, S.K. Synthesis of Nanoparticles and Their Agglomerates: Aerosol Reactors. In *R&D Status and Trends in Nanoparticles, Nanostructured Materials, and Nanodevices in the United States*; International Technology Research Institute: San Jose, CA, USA, 1998; pp. 83–88.
36. Gurav, A.; Kodas, T.; Pluym, T.; Xiong, Y. Aerosol processing of materials. *Aerosol Sci. Technol.* **1993**, *19*, 411–452. [CrossRef]
37. Zachariah, M.R.; Shull, R.D.; McMillin, B.K.; Biswas, P. In Situ Characterization and Modeling of the Vapor-Phase Formation of a Magnetic Nanocomposite. In *Proceedings of the Nanotechnology*; Koros, S.R., Duffy, J.M.O., Eds.; American Chemical Society (ACS): Washington, DC, USA, 1996; pp. 42–63. [CrossRef]
38. Kammler, H.K.; Pratsinis, S.E. Electrically-assisted flame aerosol synthesis of fumed silica at high production rates. *Chem. Eng. Process.* **2000**, *3*, 219–227. [CrossRef]
39. Rao, N.P.; Lee, H.J.; Kelkar, M.; Hansen, D.J.; Heberlein, J.W.; McMurry, P.H.; Girshick, S.L. Nanostructured materials production by hypersonic plasma particle deposition. *Nanostructured Mater.* **1997**, *9*, 129–132. [CrossRef]
40. Sarathy, K.V.; Kulkarni, G.U.; Rao, C.N. A novel method of preparing thiol-derivatised nanoparticles ofgold, platinum and silver forming superstructures. *Chem. Commun.* **1997**, *6*, 537–538. [CrossRef]
41. Lin, L.; Wang, Q. Microplasma: A new generation of technology for functional nanomaterial synthesis. *Plasma Chem. Plasma Process.* **2015**, *35*, 925–962. [CrossRef]
42. Lin, L.; Starostin, S.A.; Li, S.; Hessel, V. Synthesis of metallic nanoparticles by microplasma. *Phys. Sci. Rev.* **2018**, *3*, 20170121. [CrossRef]
43. Becker, M.F.; Brock, J.R.; Caic, H.; Henneke, D.E.; Keto, J.W.; Lee, J.; Nichols, W.T.; Glicksman, H.D. Nanoparticles generated by laser ablation. *Nanostructured Mater.* **1997**, *10*, 853–863. [CrossRef]
44. Zhang, Y.F.; Tang, Y.H.; Wang, N.; Lee, C.S.; Lee, S.T. Silicon nanowires prepared by laser ablation at high temperature. *Appl. Phys. Lett.* **1998**, *72*, 1835–1837. [CrossRef]
45. Dell'Aglio, M.; Gaudiuso, R.; De Pascale, O.; De Giacomo, A. Mechanisms and processes of pulsed laser ablation in liquids during nanoparticle production. *Appl. Surf. Sci.* **2015**, *348*, 4–9. [CrossRef]
46. Mansoureh, G.; Parisa, V. Synthesis of metal nanoparticles using laser ablation technique. In *Emerging Applications of Nanoparticles and Architecture Nanostructures*; Elsevier: Amsterdam, The Netherlands, 2018; pp. 575–596. [CrossRef]
47. Singhal, A.; Skandan, G. Production of oxide nanopowders by chemical vapor condensation. *Int. J. Powder Metall.* **1999**, *35*, 45–51.
48. Kear, B.H.; Sadangi, R.K.; McCandlish, L.E.; Voronov, O. Triphasic Composite and Method for Making SAME. Patent U.S. 6214079 B1, United States Patent and Trademark Office, 10 April 2001.
49. Harish, V.; Ansari, M.M.; Tewari, D.; Gaur, M.; Yadav, A.B.; García-Betancourt, M.L.; Abdel-Haleem, F.M.; Bechelany, M.; Barhoum, A. Nanoparticle and nanostructure synthesis and controlled growth methods. *Nanomaterials* **2022**, *12*, 3226. [CrossRef]
50. Messing, G.L.; Zhang, S.C.; Jayanthi, V.G. Ceramic powder synthesis by spray pyrolysis. *J. Am. Ceram. Soc.* **1993**, *76*, 2707–2726. [CrossRef]
51. Fisenko, S.; Khodyko, Y.A.; Penyazkov, O.; Saverchenko, V. Droplet evaporation on a substrate at the final stage of low pressure spray pyrolysis and the final morphology of nanoparticles. *Int. J. Heat Mass Transf.* **2014**, *78*, 599–603. [CrossRef]
52. Phakatkar, A.H.; Saray, M.T.; Rasul, M.G.; Sorokina, L.V.; Ritter, T.G.; Shokuhfar, T.; Shahbazian-Yassar, R. Ultrafast synthesis of high entropy oxide nanoparticles by flame spray pyrolysis. *Langmuir* **2021**, *37*, 9059–9068. [CrossRef]
53. Kastrinaki, G.; Lorentzou, S.; Karagiannakis, G.; Rattenbury, M.; Woodhead, J.; Konstandopoulos, A. Parametric synthesis study of iron based nanoparticles via aerosol spray pyrolysis route. *J. Aerosol Sci.* **2018**, *115*, 96–107. [CrossRef]
54. Oh, H.; Kim, S. Synthesis of ceria nanoparticles by flame electrospray pyrolysis. *J. Aerosol Sci.* **2007**, *38*, 1185–1196. [CrossRef]
55. Rasekh, M.; Ahmad, Z.; Cross, R.; Hernández-Gil, J.; Wilton-Ely, J.D.; Miller, P.W. Facile preparation of drug-loaded tristearin encapsulated superparamagnetic iron oxide nanoparticles using coaxial electrospray processing. *Mol. Pharm.* **2017**, *14*, 2010–2023. [CrossRef] [PubMed]
56. Liu, Y.; Li, S.; Li, H.; Hossen, M.A.; Sameen, D.E.; Dai, J.; Qin, W.; Lee, K. Synthesis and properties of core-shell thymol-loaded zein/shellac nanoparticles by coaxial electrospray as edible coatings. *Mater. Des.* **2021**, *212*, 110214. [CrossRef]
57. Karthikeyan, J.; Berndt, C.C.; Tikkanen, J.; Reddy, S.; Herman, H. Plasma spray synthesis of nanomaterial powders and deposits. *Mater. Sci. Eng.* **1997**, *238*, 275–286. [CrossRef]

58. Lee, D.; Yun, S.; Han, J.W.; Song, M.; Kim, Y.; Lee, J.; Choi, J.; Chang, S.; Hong, S.; Kim, J. Microstructural evolution and mechanical properties of atmospheric plasma sprayed Y2O3 coating with state of in-flight particle. *Ceram. Int.* **2021**, *47*, 3853–3866. [CrossRef]
59. Nava-Avendaño, J.; Veilleux, J. Plasma processes in the preparation of lithium-ion battery electrodes and separators. *J. Phys. Appl. Phys.* **2017**, *50*, 163001. [CrossRef]
60. Chiganova, G.A. Detonation synthesis of ultrafine alumina. *Inorg. Mater.* **2004**, *41*, 468–475. [CrossRef]
61. Silva, J.; Antunes, E. Ceramic Powders with a Nanoparticle Layer and Process for Obtaining Thereof. Australia AU 2008364348, 15 May 2010.
62. Silva, J.; Antunes, E. Nanometric-Sized Ceramic Materials, Process for Their Synthesis and Uses Thereof. International WO2009144665A2, 15 May 2009.
63. Langenderfer, M.J.; Fahrenholtz, W.G.; Chertopalov, S.; Zhou, Y.; Mochalin, V.N.; Johnson, C.E. Detonation Synthesis of Silicon Carbide Nanoparticles. *Ceram. Int.* **2020**, *46*, 6951–6954. [CrossRef]
64. Jamkhande, P.G.; Ghule, N.W.; Bamer, A.H.; Kalaskar, M.G. Metal nanoparticles synthesis: An overview on methods of preparation, advantages and disadvantages, and applications. *J. Drug Deliv. Sci. Technol.* **2019**, *53*, 101174. [CrossRef]
65. Ndolomingo, M.J.; Bingwa, N.; Meijboom, R. Review of supported metal nanoparticles: Synthesis methodologies, advantages and application as catalysts. *J. Mater. Sci.* **2020**, *55*, 6195–6241. [CrossRef]
66. Pareek, V.; Bhargava, A.; Gupta, R.; Jain, N.; Panwar, J. Synthesis and applications of noble metal nanoparticles: A review. *Adv. Sci. Eng. Med.* **2017**, *9*, 527–544. [CrossRef]
67. Ulrich, G.D. Theory of particle formation and growth in oxide synthesis flames. *Combust. Sci. Technol.* **1971**, *4*, 47–57. [CrossRef]
68. Pratsinis, S.; Vemury, S. Particle formation in gases: A review. *Powder Technol.* **1996**, *88*, 267–273. [CrossRef]
69. Schaefer, D.W.; Hurd, A.J. Growth and structure of combustion aerosols: Fumed silica. *Aerosol Sci. Technol.* **1990**, *12*, 876–890. [CrossRef]
70. Pratsinis, S.E.; Spicer, P.T. Competition between gas phase and surface oxidation of $TiCl_4$ during synthesis of TiO_2 particles. *Chem. Eng. Sci.* **1998**, *53*, 1861–1868. [CrossRef]
71. Fuchs, N.A.; Daisley, R.E.; Fuchs, M. *The Mechanics of Aerosols*; Dover Publications: New York, NY, USA, 1989.
72. Hinds, W.C. *Aerosol Technology: Properties, Behavior, and Measurement of Airborne Particles*, 2nd ed.; Wiley-Interscience: New York, NY, USA, 1999. [CrossRef]
73. Koch, W. The effect of particle coalescence on the surface area of a coagulating aerosol. *J. Colloid Interface Sci.* **1990**, *140*, 419–427. [CrossRef]
74. Johannessen, T.; Pratsinis, S.E.; Livbjerg, H. Computational fluid-particle dynamics for the flame synthesis of alumina particles. *Chem. Eng. Sci.* **2000**, *55*, 177–191. [CrossRef]
75. Yang, K.; Chen, L.; Lu, J.; Geng, D.; Wu, J. Reaction mechanism of aluminum nanoparticles in explosives under high temperature and high pressure by shock loading. *Phys. Chem. Chem. Phys.* **2022**, *24*, 14552–14565. [CrossRef]
76. Okuyama, K.; Lenggoro, I.W. Preparation of nanoparticles via spray route. *Chem. Eng. Sci.* **2003**, *58*, 537–547. [CrossRef]
77. Kausar, A. *Polymer / Nanodiamond Nanocomposites: Fundamentals, Properties and Applications*; Elsevier: London, UK, 2024.
78. Kaur, N.; Prakash, C.; Bhalla, A.; Chaudhary, G.R. Nanodiamonds and other organic nanoparticles: Synthesis and surface modifications. In *Functionalized Nanomaterials I*; CRC Press: Boca Raton, FL, USA, 2020; pp. 135–160.
79. Kudryashova, O.; Petrov, E.; Kolesová, A. The growth of agglomerates in the conditions of detonation synthesis of diamond. *J. Phys. Conf. Ser.* **2020**, *1666*, 012024. [CrossRef]
80. Neves, N.; Lagoa, A.; Calado, J.; do Rego, A.B.; Fortunato, E.; Martins, R.; Ferreira, I. Al-doped ZnO nanostructured powders by emulsion detonation synthesis—Improving materials for high quality sputtering targets manufacturing. *J. Eur. Ceram. Soc.* **2014**, *34*, 2325–2338. [CrossRef]
81. Yan, H.; Zhao, T.; Li, X.; Hun, C. Synthesis of Cu-doped nano-TiO_2 by detonation method. *Ceram. Int.* **2015**, *41*, 14204–14211. [CrossRef]
82. Gibot, P.; Quesnay, F.; Nicollet, C.; Laffont, L.; Schnell, F.; Mory, J.; Spitzer, D. Detonation synthesis of ZrO_2 by means of an ammonium nitrate-based explosive emulsion. *Solid State Sci.* **2020**, *108*, 106405. [CrossRef]
83. Bukaemskii, A.A.; Avramenko, S.S.; Tarasova, L.S. Ultrafine α-Al_2O_3. Explosive Method of Synthesis and Properties. *Combust. Explos. Shock Waves* **2002**, *38*, 478–483. [CrossRef]
84. Ree, F.H.; Viecelli, J.A.; Glosli, J.N. Modeling the kinetics of carbon coagulation in explosives detonation. *J.-Comput.-Aided Mater. Des.* **1998**, *5*, 265–278. [CrossRef]
85. Friedlander, S.K. *Smoke, Dust, and Haze*; Oxford University Press: New York, NY, USA, 2000.
86. Sindhu, T.K.; Sarathi, R.; Chakravarthy, S.R. Understanding nanoparticle formation by a wire explosion process through experimental and modelling studies. *Nanotechnology* **2008**, *19*, 1–11. [CrossRef]
87. Thompson, S.M.; Gubbins, K.E.; Walton, J.P.; Chantry, R.A.; Rowlinson, J.S. A molecular dynamics study of liquid drops. *J. Chem. Phys.* **1984**, *81*, 530–542. [CrossRef]
88. Champion, Y. Gas Phase Synthesis of Nanopowders. In *Nanomaterials and Nanochemistry*; Schmid, G., Ed.; Elsevier: Oxford, UK, 2007; pp. 395–427. [CrossRef]
89. Xing, Y.; Rosner, D.E. Prediction of spherule size in gas phase nanoparticle synthesis. *J. Nanoparticle Res.* **1999**, *1*, 530–542. [CrossRef]

90. Wang, C.C.; Zhang, Z.; Ying, J.Y. Photocatalytic decomposition of halogenated organics over nanocrystalline titania. *Nanostructured Mater.* **1997**, *9*, 583–586. [CrossRef]
91. Danilenko, V.V. Specific features of synthesis of detonation nanodiamonds. *Combust. Explos. Shock Waves* **2005**, *41*, 577–588. [CrossRef]
92. Liang, Z.; Browne, S.; Deiterding, R.; Shepherd, J.E. Detonation front structure and the competition for radicals. *Proc. Combust. Inst.* **2007**, *31*, 2445–2453. [CrossRef]
93. Bdzil, J.B.; Stewart, D.S. The dynamics of detonation in explosive systems. *Annu. Rev. Fluid Mech.* **2006**, *39*, 263–292. [CrossRef]
94. Benselama, A.M.; William-Louis, M.J.; Monnoyer, F. A 1D-3D mixed method for the numerical simulation of blast waves in confined geometries. *J. Comput. Phys.* **2009**, *228*, 6796–6810. [CrossRef]
95. Mader, C.L. *Numerical Modeling of Explosives and Propellants*; CRC Press: Boca Raton, FL, USA, 2008. [CrossRef]
96. Fickett, W.; William, C.D. *Detonation: Theory and Experiment*; Dover Publications: Mineola, NY, USA, 1979.
97. Davidson, L. *Fundamentals of Shock Wave Propagation in Solids*; Springer: Berlin/Heidelberg, Germany, 2008. [CrossRef]
98. Campos, J.; Mendes, R.; Calado, J.; Antunes, E.; Durães, L.; Portugal, A.; Andrade-Campos, A. Predicted Kinetic Mechanisms of Ceramic Formation from Detonation of Metal/Nitrate Compositions. In Proceedings of the 12th International Conference on Combustion and Energy Utilization, Karlsruhe, Vienna, Austria, 14–17 April 2009; pp. 123–130.
99. Merzhievskii, L.A.; Filimonov, V.A. Asymptotic curve of the scattering of the products of a steady-state detonation. *J. Appl. Mech. Tech. Phys.* **1977**, *18*, 177–182. [CrossRef]
100. Pruuél, E.R.; Merzhievskii, L.A.; Ten, K.A.; Zubkov, P.I.; Luk'yanchikov, L.A.; Tolochko, B.P.; Kozyrev, A.N.; Litvenko, V.V. Density distribution of the expanding products of steady-state detonation of TNT. *Combust. Explos. Shock Waves* **2007**, *43*, 355–364. [CrossRef]
101. Povarnitsyn, M.; Khishchenko, K.; Levashov, P. Simulation of shock-induced fragmentation and vaporization in metals. *Int. J. Impact Eng.* **2008**, *35*, 1723–1727. [CrossRef]
102. Esen, S.; Souers, P.C.; Vitello, P. Prediction of the non-ideal detonation performance of commercial explosives using the DeNE and JWL++ codes. *Int. J. Numer. Methods Eng.* **2005**, *64*, 1889–1914. [CrossRef]
103. Wood, W.W.; Kirkwood, J.G. Diameter Effect in Condensed Explosives. The Relation between Velocity and Radius of Curvature of the Detonation Wave. *J. Chem. Phys.* **1954**, *22*, 1920–1924. [CrossRef]
104. Lu, J.P.; Dorsett, H.E.; Franson, M.D.; Cliff, M.D. *Near-Field Performance Evaluations of Alex Effect in Metallised Explosives*; Technical Report DSTO-TR-1585; DSTO Systems Sciences Laboratory: Edinburgh, South Australia, 2003.
105. Evans, M.W.; Ablow, C.M. Theories of detonation. *Chem. Rev.* **1961**, *61*, 129–178. [CrossRef]
106. Menikoff, R.; Lackner, K.S.; Johnson, N.L.; Colgate, S.A.; Hyman, J.M.; Miranda, G.A. Shock wave driven by a phased implosion. *Phys. Fluids Fluid Dyn.* **1991**, *3*, 201–218. [CrossRef]
107. Khmel, T.A.; Fedorov, A.V. Modeling of plane detonation waves in a gas suspension of aluminum nanoparticles. *Combust. Shock Waves* **2018**, *54*, 189–199. [CrossRef]
108. Souers, P.C.; Garza, R. Kinetic Information from Detonation Front Curvature. Technical Report LLNL-TR-406576, Lawrence Livermore National Laboratory, Livermore, CA, USA, 1998.
109. Lee, J.H.S. *The Detonation Phenomenon*; Cambridge University Press: Cambridge, UK, 2008. [CrossRef]
110. Urtiew, P.A.; Hayes, B. Parametric study of the dynamic JWL-EoS for detonation products. *Combust. Explos. Shock Waves* **1991**, *27*, 505–514. [CrossRef]
111. Souers, P.C.; Haselman, L.C., Jr. *Detonation Equation of State at LLNL*; Technical report; Lawrence Livermore National Laboratory, Energetic Materials Center: Livermore, CA, USA, 1993. [CrossRef]
112. Landau, L.D.; Lifshitz, M.C. *Fluid Mechanics*, 2nd ed.; Pergamon Press: New York, NY, USA, 1987. [CrossRef]
113. Saurel, R.; Massoni, J. On Riemman-problem-based methods for detonations in solid energetic materials. *Int. J. Numer. Methods Fluids* **1998**, *26*, 101–121. [CrossRef]
114. Massoni, J.; Saurel, R.; Lefrançois, A.; Baudin, G. Modeling spherical explosions with aluminized energetic materials. *Shock Waves* **2006**, *16*, 75–92. [CrossRef]
115. Davis, L.L.; Hill, L.G. ANFO Cylinder Tests. In Proceedings of the Proceedings of the Conference on Shock Compression of Condensed Matter, Anaheim, CA, USA, 10–15 July 2022; pp. 165–168. [CrossRef]
116. Sturgeon, J.; Thomas, R.M.; Gladwell, I. Solving a singular DAE model of unconfined detonation. *Comput. Chem.* **2001**, *25*, 83–95. [CrossRef] [PubMed]
117. Fickett, W.; Wood, W.W. A detonation-product equation of state obtained from hidrodynamic data. *Phys. Fluids* **1958**, *1*, 528–534. [CrossRef]
118. Menikoff, R. Comparison of constitutive models for plastic-bonded explosives. *Combust. Theory Model.* **2008**, *12*, 73–91. [CrossRef]
119. Ahuja, R.; Belonoshko, A.B.; Johansson, B. Melting and liquid structure of aluminum oxide using a molecular-dynamics simulation. *Phys. Rev. E* **1998**, *57*, 1673–1676. [CrossRef]
120. Teteris, G.; Briedis, I. A contribution to the sintering model of viscoelastic liquid drops with solid kernels. *Mech. Compos. Mater.* **1997**, *33*, 397–401. [CrossRef]
121. Hammons, J.A.; Nielsen, M.H.; Bagge-Hansen, M.; Bastea, S.; Shaw, W.L.; Lee, J.R.; Ilavsky, J.; Sinclair, N.; Fezzaa, K.; Lauderbach, L.M.; et al. Resolving detonation nanodiamond size evolution and morphology at sub-microsecond timescales during high-explosive detonations. *J. Phys. Chem. C* **2019**, *123*, 19153–19164. [CrossRef]

122. Azizi, F.; Al Taweel, A.M. Algorithm for the accurate numerical solution of PBE for drop breakup and coalescence under high shear rates. *Chem. Eng. Sci.* **2010**, *65*, 6112–6127. [CrossRef]
123. Hulburt, H.; Katz, S. Some problems in particle technology: A statistical mechanical formulation. *Chem. Eng. Sci.* **1964**, *19*, 555–574. [CrossRef]
124. Randolph, A. *Theory of Particulate Processes: Analysis and Techniques of Continuous Crystallization*; Academic Press: New York, NY, USA, 1971.
125. Ramkrishna, D. The status of Population Balances. *Rev. Chem. Eng.* **1985**, *3*, 49–95. [CrossRef]
126. Ramkrishna, D. *Population Balances: Theory and Applications to Particulate Systems in Engineering*; Academic Press: New York, NY, USA, 2000.
127. Kumar, S.; Ramkrishna, D. On the solution of population balances equations by discretization-I. A fixed pivot technique. *Chem. Eng. Sci.* **1996**, *51*, 1311–1332. [CrossRef]
128. Kumar, S.; Ramkrishna, D. On the solution of population balances equations by discretization-II. A moving pivot technique. *Chem. Eng. Sci.* **1996**, *51*, 1333–1342. [CrossRef]
129. Bird, G.A. *Molecular Gas Dynamics and the Direct Simulation of Gas Flows*; Oxford University Press: New York, NY, USA, 1994.
130. Shaw, M.S.; Johnson, J.D. Carbon clustering in detonations. *J. Appl. Phys.* **1987**, *62*, 2080–2085. [CrossRef]
131. Puel, F.; Févotte, G.; Klein, J. Simulation and analysis of industrial crystallization processes through multidimensional population balance equations. Part 1: A resolution algorithm based on the method of classes. *Chem. Eng. Sci.* **2003**, *58*, 3715–3727. [CrossRef]
132. Alvarez, J.; Alvarez, J.; Hernández, M. A population balance approach for the description of particle size distribution in suspension polymerization reactors. *Chem. Eng. Sci.* **1994**, *49*, 99–113. [CrossRef]
133. Chatzi, E.G.; Kiparissides, C. Dynamic simulation of bimodal drop size distributions in Low-Coalescence batch dispersion systems. *Chem. Eng. Sci.* **1992**, *47*, 445–456. [CrossRef]
134. Chen, M.Q.; Hwang, C.; Shih, Y.P. A wavelet-Galerkin method for solving population balance equations. *Comput. Chem. Eng.* **1996**, *20*, 131–145. [CrossRef]
135. Gelbard, F.; Seinfeld, J. Simulation of multicomponent aerosol dynamics. *J. Colloid Interface Sci.* **1980**, *78*, 485–501. [CrossRef]
136. Hounslow, M.J.; Ryall, R.L.; Marshall, V.R. A discretized population balance for nucleation, growth, and aggregation. *AIChE J.* **1988**, *34*, 1821–1832. [CrossRef]
137. Kiparissides, C. Polymerization reactor modeling: A review of recent developments and future directions. *Chem. Eng. Sci.* **1996**, *51*, 1637–1659. [CrossRef]
138. Nicmanis, M.; Hounslow, M.J. Finite-element methods for steady-state population balance equations. *AIChE J.* **1998**, *44*, 2258–2272. [CrossRef]
139. Singh, P.; Ramkrishna, D. Transient solution of the brownian coagulation equation by problem-specific polynomials. *J. Colloid Interface Sci.* **1975**, *53*, 214–223. [CrossRef]
140. Singh, P.N.; Ramkrishna, D. Solution of population balance equations. *Comput. Chem. Eng.* **1977**, *1*, 23–31. [CrossRef]
141. Sewerin, F.; Rigopoulos, S. An explicit adaptive grid approach for the numerical solution of the population balance equation. *Chem. Eng. Sci.* **2017**, *168*, 250–270. [CrossRef]
142. O'Sullivan, D.; Rigopoulos, S. A conservative finite volume method for the population balance equation with aggregation, fragmentation, nucleation and growth. *Chem. Eng. Sci.* **2022**, *263*, 117925. [CrossRef]
143. Duarte, B.P.; Baptista, C.M. Moving finite elements method applied to dynamic population balance equations. *AIChE J.* **2008**, *54*, 673–692. [CrossRef]
144. Nopens, I.; Vanrolleghem, P. Comparison of discretization methods to solve a population balance model of activated sludge flocculation including aggregation and breakage. *Math. Comput. Model. Dyn. Syst.* **2006**, *12*, 441–454. [CrossRef]
145. Wolfram Research Inc. *Mathematica, Version 14.1.*; Wolfram Research Inc.: Champaign, IL, USA, 2024.
146. Hindmarsh, A.C.; Taylor, A.G. *User Documentation for IDA: A Differential-Algebraic Equation Solver for Sequential and Parallel Computers*; Technical Report UCRL-MA-132042; Lawrence Livermore National Laboratory: Livermore, CA, USA, 1999.
147. Durães, L.; Campos, J.; Portugal, A. Reaction path of energetic materials using `THOR` code. *AIP Conf. Proc.* **1998**, *429*, 341–344. [CrossRef]
148. Arienti, M.; Morano, E.; Shepherd, J.E. *Shock and Detonation Modeling with the Mie-Grüneisen Equation of State*; Technical Report Caltech-1234; California Institute of Technology: Pasadena, CA, USA, 2004.
149. Fried, L.E.; Howard, W.M.; Souers, P.C.; Haselman, L. *Adding Kinetics and Hydrodynamics to the CHEETAH Thermochemical Code*; Technical Report UCRL-ID-125830; Lawrence Livermore National Laboratory: Livermore, CA, USA, 1997.
150. Tarver, C.M.; Urtiew, P.A. *Theoretical and Computer Models of Detonation in Solid Explosives*; Technical Report UCRL-ID-126467; Lawrence Livermore National Laboratory: Livermore, CA, USA, 1997.
151. Lu, J.P. *Evaluation of the Thermochemical Code—CHEETAH 2.0 for Modelling Explosives Performance*; Technical Report DSTO-TR-1373; Department of Defence—Defence Science & Technology Organisation: Melbourne, Australia, 2001.
152. McCullagh, P.; Nelder, J.A. *Generalized Linear Models*, 2nd ed.; Chapman and Hall/CRC: New York, NY, USA, 1989.